Master’s thesis
Meteorology

The impact of aerosols on the sensible and latent heat fluxes in Beijing

Sonja Murto

2017

Supervisor: Dos. Leena Järvi

Reviewers:
Dos. Leena Järvi
Prof. Heikki Järvinen

UNIVERSITY OF HELSINKI
FACULTY OF SCIENCES
DEPARTMENT OF PHYSICS

PL 64 (Gustaf Hällströmin katu 2)
00014 Helsingin yliopisto

HELSINGIN YLIOPISTO – HELSINGFORS UNIVERSITET – UNIVERSITY OF HELSINKI

Tiedekunta/Osasto – Fakultet/Sektion – Faculty/Section	Laitos – Institution – Department
Matematisk-naturvetenskapliga fakulteten	Institutionen för fysik

Tekijä – Författare – Author
Sonja Murto

Työn nimi – Arbetets titel – Title
Aerosolernas inverkan på sensibla och latenta värmeflöden i Beijing

Oppiaine – Läroämne – Subject
Meteorologi

Työn laji – Arbetets art – Level	Aika – Datum – Month and year	Sivumäärä – Sidoantal – Number of pages
Magisteravhandling	10/17	55

Tiivistelmä – Referat – Abstract

Antropogena utsläpp har ökat i och med snabb urbanisering och industrialisering, vilket har skett under de senaste årtionden och gett upphov till dålig luftkvalitet, speciellt i utvecklingsländer, så som in Kina. Dålig luftkvalitet ökar både miljörisker samt orsakar allmänna hälsoproblem, vilket tillsammans med klimatinverkan av aerosoler ökar intresset hos forskare att förstå aerosol partiklar samt hur de påverkar vår omgivning. Ett välkänt fenomen är hur aerosoler påverkar nettostrålningen vid markytan, medan oklarheter uppstår gällande hur de inverkar på de turbulenta energitermerna, som består av sensibla och latenta värmeflöden. Med hjälp av en enkel modell (SUEWS), som kan simulera de olika energitermerna i urbana miljöer, tillsammans med aerosoldata (Aerosol Optical Depth, AOD) från Beijing, försöker jag i min studie utvidga kunskapen gällande aerosolernas inverkan på alla energitermer. Modellen är kompetent att simulera dessa termer med hjälp av allmänna meteorologiska data för forskningsperioden 2006–2009, samt parametrar som på det bästa möjliga sättet motsvarar forskningsområdet, som omfattar en cirkel med 1 km radie runt det meteorologiska tornet i Beijing. För vidare dataanalys delas data i termiska årstider samt i föroreningskategorier enligt tillgänglig AOD-data. Förhållanden med extremt förorenad luft påträffas för 24 % av studietiden. Graden av hur förorenad luften är varierar per årstid, då förhållanden med dålig luftkvalitet förekommer till endast 8 % på vintern jämfört med 27 % under sommaren. Syftet med mitt arbete är därmed att analysera till hur stor grad aerosolpartiklar påverkar de olika energitermerna i markytans energibalans, med speciell betoning gällande de turbulenta termerna.

Modellen utvärderas med hjälp av observerade värden av turbulenta energitermerna erhållna av mätningar vid tornet i Beijing. Fastän modellen tydligt övervärderar sensibla värmeflödet och undervärderar latenta värmeflödet, visar det sig att modellen dock klarar av att återskapa dygnsvariationen av energitermerna väl. Beteendet av de simulerade energitermerna undersöks, vilket även framhäver hur termerna tydligt varierar per månad. Klimatet i Beijing, kännetecknat med torr (november till april)- och regnperioder (maj till oktober), bestämmer i stort sett hur de olika turbulenta termerna förhåller sig till varandra. Förnimbara värmeflödet dominerar i mars och står för 59 % av energin som finns tillgängligt, medan en större del av energin förbrukas av latenta värmeflödet under regnperioder (61 % i augusti). Då aerosolernas inverkan tas i beaktan, visar resultaten av denna studie hur nettostrålningen tydligt minskar vid sämre luftförhållanden (maximalt 138 W/m2 skillnad mellan rena och förorenade förhållanden). Huvudforskningsresultatet är dock att aerosolerna även tydligt påverkar de turbulenta energitermerna. Aerosoler påverkar sensibla värmeflödet mest under våren (66 W/m2 skillnad) då även största delen av energin som är tillgängligt förbrukas av samma term. Samma trend påträffas även hos latenta värmeflödet, där aerosolernas inverkan är tydligast på sommaren (25 W/m2 skillnad). Studien framhäver hur viktigt det är att bibehålla information gällande aerosolkoncentrationer i luften samt deras egenskaper i urbana miljöer, eftersom aerosoler inte bara påverkar nettostrålningen, men också alla andra termer i markytans energibalans och kan därmed vidare påverka vattencirkulationen samt öka andra miljörisker i tättbefolkade urbana områden. Resultaten av denna studie kan ytterligare användas som hjälp i urban planering samt ärenden gällande vattenförvaltning och reglering av luftutsläpp.

Avainsanat – Nyckelord – Keywords
urbana markytans energibalans, luftutsläpp, turbulenta värmeflöden, modellprestation, miljonstad

Säilytyspaikka – Förvaringställe – Where deposited
Vetenskapsbiblioteket på Gumtäkt

Muita tietoja – Övriga uppgifter – Additional information

HELSINGIN YLIOPISTO – HELSINGFORS UNIVERSITET – UNIVERSITY OF HELSINKI

Tiedekunta/Osasto – Fakultet/Sektion – Faculty/Section Faculty of Sciences	Laitos – Institution – Department Department of Physics

Tekijä – Författare – Author

Sonja Murto

Työn nimi – Arbetets titel – Title

The impact of aerosols on the sensible and latent heat fluxes in Beijing

Oppiaine – Läroämne – Subject

Meteorology

Työn laji – Arbetets art – Level Master's thesis	Aika – Datum – Month and year 10/17	Sivumäärä – Sidoantal – Number of pages 55

Tiivistelmä – Referat – Abstract

In recent decades, rapid urbanization together with industrialization has led to an increase in anthropogenic emissions, resulting in high air pollution concentrations and poor air quality particularly in developing countries, such as in China. Due to both the enhanced environmental and severe public health risks poor air quality is causing and the climate impacts of aerosols, it is of great interest to study and understand aerosol particles and their impact on our surroundings. Aerosols affect the radiative properties of the atmosphere and the surface energy balance. The impact of aerosols on the surface radiative fluxes of the urban surface energy balance is widely known, but the impact on the turbulent energy fluxes, which are important components in the energy balance, has until now remained unclear. To extend the knowledge of aerosol impacts on all the energy balance components, a simple urban land surface model (SUEWS) during the period of 2006-2009 is used, together with aerosol data, Aerosol Optical Depth (AOD), received from an AERONET station located in Beijing. With the use of commonly measured meteorological variables together with parameters defined for the study area of 1 km radius around a meteorological tower, the components of the urban surface energy balance are simulated by the model. For further data analysis, the data are divided into thermal seasons and pollutant categories according to the available AOD-data. Extreme polluted conditions are achieved during 24 % for the time of available AOD-data, additionally showing relatively less situations with poor air quality (8 %) in winter compared to 27 % observed in summer. The aim of this study is to analyse how much aerosol particles can modify the different surface energy balance components, particularly focusing on the turbulent fluxes.

The model is evaluated against observed turbulent fluxes in the same tower, showing an overestimation of the sensible heat flux and an underestimation and a better model performance of the latent heat flux. Still, the diurnal behaviour of the fluxes is shown to be well reproduced by the model. The behaviour of the modelled components is further investigated, showing a clear monthly variation for almost all the fluxes contributing to the surface energy balance. The behaviour of the total energy balance is in general controlled by the wet (occurring from May to October) and dry periods, distinguishing the climate in Beijing. The sensible heat flux is the dominant flux in March, accounting for 59 % of the available energy, whereas during the wet periods, higher portion of the available energy is consumed by the turbulent latent heat flux (61 % in August). Adding the effect of aerosols, the results clearly show how the net radiative flux is decreased in poor air quality conditions, giving differences of 138 W/m2 in the median flux due to aerosol loading in the atmosphere. The main finding of this study is that aerosols also influence the turbulent fluxes, with largest aerosol impact on the sensible heat flux occurring during thermal spring (66 W/m2 difference between clean and polluted air conditions). Likewise, in summer, when the latent heat flux is the largest contributor for consuming the available energy, the influence of aerosols is most visible (25 W/m2 difference). This study highlights the importance of maintaining measurements of aerosol concentrations and characteristics of the pollutants over urban areas due to their influence not only on the radiative fluxes, but all the components of the surface energy balance, which can further alter the water circulation and give rise to other environmental risks. These findings can therefore be used in urban planning and issues related to water management and air pollution regulations.

Avainsanat – Nyckelord – Keywords

urban surface energy balance, air pollution, turbulent energy fluxes, model performance, mega-city

Säilytyspaikka – Förvaringställe – Where deposited

Kumpula science library

Muita tietoja – Övriga uppgifter – Additional information

Contents

1 Introduction

The number of people living in urban areas has been rapidly increasing during the past decades. In 1950, only 30 % of the world's population lived in cities, but the number of urban dwellers exceeded the global rural population already in 2007. In 2050, the relation is expected to be almost reverse to 100 years before, so that 66 % of the world population would live in urban areas (United Nations, 2014). The global urbanization has also been seen in China. In 1950, the relation between rural-urban population was 90−10 %, which remarkably differed from the global values. The proceeding urbanization has been, on the other hand, remarkably rapid, resulting in equal relations already in 2010. In 2050, the rural-urban relation is predicted to be higher than globally, when four-fifth of the population in China will be living in cities (United Nations, 2014). Urbanization, especially the land use changes and increased human energy supply, has a huge impact on the energy and water exchanges between the atmosphere and the surface. Less vegetated surfaces lead to decrease in the total evapotranspiration (Xiao et al., 2007) and increased area of impervious surfaces lead to reduced infiltration and soil storage capacity, both of which result in greater risk of floods (Rodriguez et al., 2003). Furthermore, the energy and radiation exchanges at the surface are altered and higher surface temperatures and sensible heat emissions to the atmosphere are expected in cities compared to the surrounding regions (Oke, 1982). Additionally, urban buildings operate as additional heat sources for cities.

The anthropogenic activities do not only involve increased human energy supply and changes in the surface cover, but urbanization also means increased amount of air pollutants through increased traffic, industrialization and general consumption (e.g. Shao et al., 2006). Aerosols, airborne solid or liquid particles, modify radiation transfer both indirectly through clouds and directly by either scattering, absorbing and re-emitting both longwave (LW) and shortwave (SW) radiation. Thus, they also affect the surface energy balance (SEB) by contributing to the energy and water exchanges between the urban surface and the atmosphere (Lamb and Verlinde, 2011). Previous studies have shown how an increase in atmospheric aerosols alters the radiation budget and thereby the energy balance in urban areas (e.g. Estournel et al., 1983; Nair et al., 2011). Pollutants also affect the thermal structure of the atmosphere and are shown to be one of the causes for elevated inversions seen over urban areas due to the infrared pollutant absorbers (Atwater, 1971; Petäjä et al., 2016).

The human activities are increasing through the ongoing urbanization, leading to higher aerosol emissions and land cover modifications. Due to urbanization, also a larger share of the surface is categorized as urban. Thus, more people are and will be affected by the climate and weather in urban areas, highlighting the need for accurate forecasts, climate information and urban planning (Grimmond et al., 2010). In areas, where aerosols have become a serious environmental problem, their effect on the climate is of most interest. There is a growing concern on what kind of effect the increasing amount of air pollutants have on the urban environment, particularly due to their severe effects on human health or lives and, furthermore, what kind of role aerosols have on the global climate. Knowledge about the exchange of water and heat between surface and atmosphere in urban areas needs to be well understood to be able to qualify the different climate effect in urban areas (Mitchell et al., 2008) and to determine how vulnerable urban areas are for these processes and risks. The aim of land surface models is to simulate, parameterize and examine these surface-atmosphere interactions (Grimmond et al., 2010). Although there are many hydrological models developed to simulate urban runoff and drainage (e.g. Mitchell et al., 2008), most land surface models lack the connection to water cycles especially in urban areas. Land surface models that simulate both water and energy exchanges between the surface and atmosphere can be used to quantify the effect of urbanization to the climate system and vice versa. Furthermore, these models are vital in urban planning concerning decisions about water restrictions and management, heat related issues as well as to examine the role of pollutants on the climate.

Previous studies mostly highlight the aerosol radiative effects (e.g. Rouse et al., 1973; Estournel et al., 1983), which include e.g. decreased global temperatures over polluted areas through attenuation of incoming solar radiation and an excess in downward infrared radiation due to aerosols increasing the downward longwave radiation. However, less research has been done concerning the aerosol impact on the different components of the surface energy balance (SEB). In this study, aerosols are discusses and the main question I want to answer is that how much aerosol particles can modify the different SEB components in polluted Beijing, China. A simple urban land surface model (SUEWS) together with aerosol data measured in Beijing during the period 2006−2009 are used to evaluate the aerosol impact particularly on the turbulent fluxes, which are important components in the SEB. A general description of aerosols, the different components in the SEB as well as some discussion about the model challenges are provided in Chapter 2. The SUEWS model, site description and other additional data and methods used for this study are presented in Chapter 3. Results and discussion are presented in Chapter 4 and finally, a summary is provided in Chapter 5.

2 Theory

2.1 Surface energy balance

The exchange of energy between the surface of the Earth and the overlying atmosphere and processes related to it regulate and control air temperatures and mixing of air in the atmosphere, and further control the water circulation and determine the surface temperature. Hence, studying the processes concerning energy exchanges is important and of great interest. The general surface energy balance (SEB) equation (2.1) is a sum of four radiative fluxes, two turbulent fluxes and the ground heat flux. All the energy components and radiation components are in units of W m^{-2}. The SEB- equation can be written as:

$$SEB = Q^{*} - Q_E - Q_H - \Delta Q_S = 0, \tag{2.1}$$

where Q^{*} is the net all-wave radiation, Q_E is the latent heat flux, Q_H is the turbulent sensible heat flux and ΔQ_S represents the net storage heat flux. The turbulent fluxes involve energy related to water phase changes as well as surface heating. The net all-wave radiation consists of four radiation components: incoming ($K\downarrow$) and outgoing ($K\uparrow$) shortwave (SW) radiation as well as the same for longwave (LW) radiation and is modelled as:

$$Q^{*} = (K\downarrow - K\uparrow) + (L\downarrow - L\uparrow). \tag{2.2}$$

According to Wallace and Hobbs (2006), when assuming that all the fluxes are acting on a thin infinite layer at the interface between the atmosphere and the surface, later treated as the surface, for a longer time average, the net SEB must be equal to zero (Equation 2.1). In other words, the energy input to the system must equal the energy output. When the terms are positive the surface gains energy, whereas negative terms represent a less of energy for the surface. Instead of representing the SEB as a sum of terms that equal zero (2.1), it can also be written in a different way. Here the terms are separated so that the terms on the left-hand side stand for the energy supply that will be shared differently depending on the prevailing conditions, among the terms written on the right-hand side of the equal sign (see Equation 2.3).

When looking more in detail on the energy budget in urban environments, other input sources should be taken into consideration. In urban areas, the surface energy budget is also influenced by human energy consumption that give rise to anthropogenic sensible heat and moisture emissions into the atmosphere (Sailor, 2011). The sources of the anthropogenic heat emissions can further be divided into three main sectors: industry, buildings and transportation through vehicle emissions. The heat release due to anthropogenic activities also include moisture emissions, as by-product in chemical reactions or as evaporated water, and due to water being the most important greenhouse gas, it has furthermore impact on the LW radiation budget. Industries are rather stationary and contribute to a more even energy distribution, whereas the emissions caused by vehicles are more spatially and temporally dependent. Additionally, the heat from buildings depends on both climate and human daily routines and activities. During winter, the anthropogenic heat flux is mostly dominated by building heating, whereas the vehicle sector is a large contributor during rush hours (Bergeron and Strachan, 2012). Notable is that the energy consumption as well as the relative importance of each sector varies in different countries and cities, but nevertheless, all the different sectors need to be taken into consideration when simulating the anthropogenic heat flux (Lindberg et al., 2013). Figure 1 illustrates the main concept of the fluxes included in the urban surface energy balance.

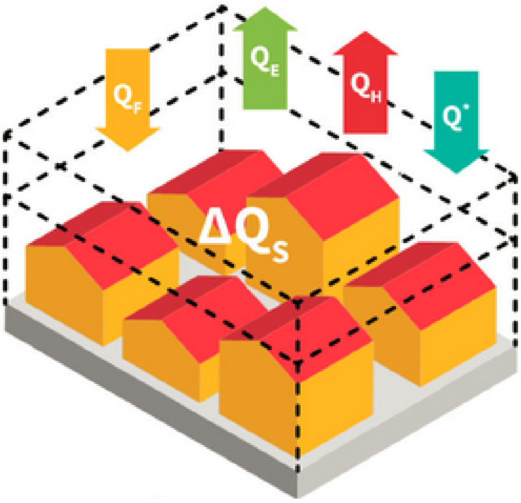

Figure 1. Schematic sketch to illustrate the urban surface energy balance (modified from CORDIS, 2016).

When including Q_F to the SEB equation (2.1), the urban energy balance gets the following form (Oke, 1982):

$$Q^* + Q_F = Q_E + Q_H + \Delta Q_S, \tag{2.3}$$

where the available energy consists of both Q^* and additionally Q_F, the anthropogenic heat flux. This available energy or energy supply is then shared between the variables on the right-hand side of the energy balance equation: the turbulent fluxes Q_H and Q_E and also ΔQ_S, including soil heat flux and heat stored and released to urban constructions. The storage heat flux is shown as the total change in the storage heat flux, labelled as ΔQ_S.

The urban energy balance is further linked to the urban water balance through evaporation (E) via the latent heat flux Q_E (=$L_v E$, where L_v is the latent heat of evaporation). The urban water balance can be written as (Grimmond et al., 1986):

$$P + I_E = E + R + \Delta S, \tag{2.4}$$

where P is precipitation (rain or snowfall), I_E is the water that is supplied to the system through water pipes via irrigation or street cleaning. This water supply to the urban system is shared between the components on the right-hand side: evaporation, R is runoff (both deep soil and above-ground runoff) and ΔS stands for the net change in water storage (here also including changes in soil moisture and water kept on the surface). The water components are in units of mm h^{-1}.

2.1.1 Determining the components of the surface energy balance

The urban SEB equation (2.3) consists of different components and information about all the components need to be obtained in order to understand the total energy exchange between the surface and the atmosphere. There are different techniques for the determination of the components. The eddy covariance (EC) technique is a preferred method for the turbulent fluxes, as it measures net exchange between the surface and the atmosphere. It has been commonly used to estimate the fluxes of CO_2, energy and water between the atmosphere and vegetation (Baldocchi, 2003). Furthermore, the net radiation flux Q^* can be measured with radiometers that measure the four radiation components in 2.2. However, the remaining two components, the ΔQ_S the Q_F, can't be directly measured, which highlights the need for numerical models to close all fluxes.

Today there are many different urban land surface models (LSMs) created to model the exchange between the surface and atmosphere and to calculate and reproduce additional features related to urban areas. The models differ slightly from each other depending on the model assumptions, parametrizations and parameters, as well as having different requirements for input parameters, timeseries of forcing data and information on initial conditions (Grimmond et al., 2010). The main requirement for urban LSMs incorporated in atmospheric models is that they, based on these input data, can simulate all the components of the surface energy balance equation, particularly in urban areas. Additionally, LSMs are vital in obtaining information from areas when observations are missing and they are generally necessary to provide information concerning the past or the future. Grimmond et al. (2010, 2011); Demuzere et al. (2017); Karsisto et al. (2016) evaluated different LSMs, showing that none of the models perform best in simulating all fluxes, and differences in model performance between day and night as well as between individual fluxes are visible. Evaluations agreed in that models are best in simulating the net all-wave radiation, whereas the latent heat flux causes most difficulties.

The models can further be divided into four main groups depending on model property to simulate each flux: class details, turbulent flux method, urban morphology and vegetation combinations and energy balance closure (Grimmond et al., 2010). The first group includes questions concerning simulation of vegetation, anthropogenic heat flux, storage heat flux and radiative properties of the surface for calculating radiative fluxes. For example, most models calculate ΔQ_S as a residual term (Grimmond and Oke, 1999b), such as in the Community Land Model (CLM; Lawrence et al., 2011) and SURFEX (Masson et al., 2003), but alternative ways of modelling the term has been provided by Grimmond et al. (1991). They use the Objective Hysteresis Model (OHM), where the ΔQ_S is modelled from the available energy and the surface properties of the study area. The OHM coefficients for vegetated, impervious and building sites need to be determined, which is not the case when calculating the term as a residual. It is shown that the OHM method improves model performance for most study sites (e.g. Grimmond and Oke, 2002, 1999b). The second group comprises the different methods in modelling the turbulent fluxes (Q_E and Q_H), which vary between different models. Typically, surface conductance (or resistance methods) schemes are used in addition to temperature and/or moisture profiles. There are simple methods as well as more complicated ways of calculations, such as using the Penman-Monteith equation (e.g. in Järvi et al., 2011). The last group deal with whether the models force a closure of the energy balance equation, which is vital to prevent numerical instabilities or biases in long-term climate model simulations. The closure can be forced i.e. through calculating some of the SEB components as a residual (such as ΔQ_S or Q_H) or by restricting the turbulent fluxes to maintain only the energy that is available.

2.1.2 Challenges to modelling

The different processes the models want to simulate and project induce difficulties in model predictability due to their large range of temporal and spatial scales. Additionally, computational limitations when simulating the climate system easily occur and the limitations are tried to be solved with the use of parametrizations to count for processes occurring in scales smaller than the model resolution. Due to its complexity, a balance between the parametrizations and the required computation skills need to be achieved, aiming to an accurate prediction of the fluxes within the system.

The choice of model parameters is therefore challenging and impacts model performance. Which parameters should be used to obtain the best modelling result and how well do the default variables represent the reality are questions that appear when defining the model parameters. A poor choice of model parameter values can significantly decrease model performance, also in those cases when the model would otherwise perform well (Grimmond et al., 2011). Additionally, some models could perform well on the behalf of wrong physical reasons, when e.g.some energy components could be overestimated in order to maintain correct values for the turbulent fluxes. Apart from default parameters, some are site dependent and therefore relies on observations made from the site. The site-specific surface cover fractions are shown to have a huge impact on model performance. It is obvious that more accurate observations from different sites are needed in order to reduce the problems related to model parametrizations and model performance together with improved model resolution.

There are different ways of mapping the surface land cover: use of remote sensing (e.g. Running et al., 1994), using existing global databases or aerial photos that can further be digitalized using computers. Disadvantages of using databases are that they provide fixed values for certain global areas, whereas limiting factors in remote sensing are the coarse resolution and high expenses in the use of different bands for classifying land cover types (Running et al., 1994). Aerial satellite photos used as base maps in distinguishing terrestrial surface covers may contain the most precise and actual information, but disadvantages in using them can be shadows or other light-related obstacles that make the classification harder for the user.

Furthermore, the different subgrid scale processes occurring inside the model grid need proper parametrizations and the connection between them is also vital. For instance, there are many hydrological models to simulate urban runoff (e.g. Mitchell et al., 2008), but most of the land surface models lack the connection to water cycles and schemes, especially in urban areas. According to Järvi et al. (2014), this lack of connection can lead to underestimations of the latent heat flux simulated in the model and furthermore increase estimations for other heat emissions from the surface to the atmosphere.

Another challenge concerning modelling is the forcing data required for the model run. One option is to use observed meteorological data, but the downside of this is that instruments also have errors that vary with time, location and land cover. This should be kept in mind when evaluating model performance and reliability of the model output data. For instance, daily precipitation could be measured kilometres apart from the source area of a study, which itself can already cause errors due to discontinuous patterns of precipitation and spatial resolution. Furthermore, model input resolution could differ from observation resolution and the way of solving the issue should be considered carefully as all additional modifications can distort the results. Data with high resolution is often unavailable, and therefore the use of reanalysis data applied with a correction method can be used instead of observed data as the required model forcing data (Kokkonen et al., 2017).

The degree of model complexity is also another issue related to modelling. The simplest and most complex models perform better compared to models with medium complexity (Grimmond et al., 2011). Improvements can be made by increasing the amount of information given to the simple models. The more complex a model is, the harder it can be to notice possible improvements. Most complex models, on the other hand, could be more open for further improvements due to being able to resolve more precisely different problems, but as disadvantage is the complexity for the user and how easy it is to use a model. Disadvantages with more complex models can on the other hand be also the high expenses and the demand of higher computer capacity.

2.2 Aerosols and air quality

Atmospheric aerosols, liquid or solid particles suspended in the air, have an important role in contributing to different phenomena in the Earth´s atmosphere. The aerosol particles found in the atmosphere affect not only the composition of the atmosphere, but they have also an impact on the daily life of human beings by way of impacting the climate and air quality, thereby also affecting public health (Sundström et al., 2014).

Aerosols can be classified according to their size or origin. The diameter of the aerosol particles can vary from a few manometers to hundreds of micrometers, including both fine and coarse mode particles (Figure 2, Haywood and Boucher, 2000). The smallest aerosols, characterized by diameters between a few to ten nanometers, are referred as nucleation mode particles, Aitken mode particles have diameters ranging from 10 nm to 100 nm, whereas the accumulation mode particles have larger diameters up to 1 μm. If the diameter of the aerosol particle exceeds 1 μm, the particles are then referred as coarse mode particles. A more common used classification of aerosols according to their size is to divide them into fine particulate matter, $PM_{2.5}$, and coarse particles, PM_{10}, with aerodynamic diameters smaller than 2.5 μm or 10 μm, respectively (Sundström et al., 2014).

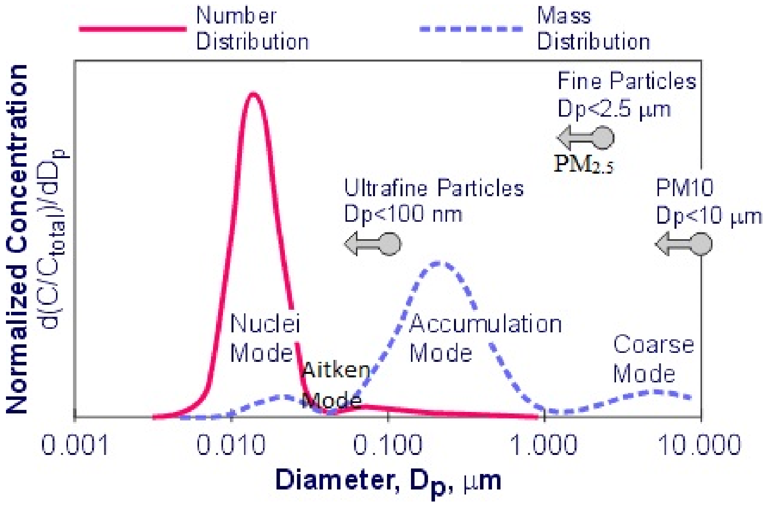

Figure 2. Aerosol particle size distribution displaying the classifications into modes as number or mass distribution and particulate matter (PM) division. The particle diameter size is shown in μm. Figure is modified from DieselNet (2002).

The second way of classification is to divide the aerosol particles into primary and secondary particles based on their origin (e.g. Haywood and Boucher, 2000). Primary particles are emitted directly to the atmosphere at their sources, that can further be divided into natural and anthropogenic sources. Sea-salt particles and mineral dust due to wind erosion on open land or originated from deserts belong to natural primary particles. Man-made particles, on the other hand, mostly originate from industrial activities, e.g. from combustion processes or diesel engines (Sundström et al., 2014). On the contrary, secondary aerosol particles are formed from a pre-existing gas through different reactions or gas conversions, such as sulphate and nitrate aerosols. These secondary particles can therefore also contain anthropogenic components, which together with black and organic carbon and mineral dust are referred as tropospheric aerosols containing anthropogenic components (Haywood and Boucher, 2000). Gas-to-particle conversions can be observed even within the free and upper troposphere, not only close to the surface (Kulmala et al., 2004). The formation rate for particles with diameters of 3 nm in industrial areas can be more than thousand times higher compared to remote areas, such as Antarctica.

Aerosols are often concentrated in the atmospheric boundary layer, the layer which is in direct interaction with the surface of the Earth. The typical number of aerosol particle concentration in the maritime boundary layer, as well as in the free troposphere, varies between $300-2000$ cm^{-3} and between $1000-10$ 000 cm^{-3} in the continental boundary layer (Spracklen et al., 2010). Depending on the atmospheric conditions and their size, aerosols can reside in the atmosphere from a few hours or days to many weeks. Additionally, aerosols can be influenced by synoptic weather systems and e.g. be blown away by a cold air current (Zheng et al., 2015), thereby being transported to places far away from the sources and consequently affecting the air quality in nearby areas. Once they are formed, aerosols can further react with other particles until they are eventually being removed from the atmosphere through wet (through precipitation of clouds) or dry deposition (Haywood and Boucher, 2000).

In order to determine the aerosol impact, information about aerosol particle properties is vital to obtain (Holben et al., 1998). These can be provided by different remote sensing instruments, either space-borne or ground-based (Sundström et al., 2014). Active instruments emit electromagnetic radiation themselves, whereas passive devices use natural sources, such as solar radiation, in order to obtain information about the aerosols. Space-borne satellite instruments measure outgoing solar radiation at the top of the atmosphere and provide only daytime observations. Another passive instrument, though ground-based, is a sunphotometer that measures the incoming solar radiation at different wavelengths. Less assumptions are needed in these ground-based passive instruments compared to the satellite instruments because of the hypothesis that only the atmosphere impacts the incoming radiation (not the Earth). Common to these two different passive instruments is that the observations are based on column integrated aerosol extinction, that is, how much radiation is getting through and how much is not due to the aerosols in the column. Therefore, these observations can be made only at cloud-free skies, due to the need of sunlight. AOD, the aerosol optical depth, is the most common aerosol parameter from remote sensing instruments and describes quantitatively the extinction of sunlight by aerosols, integrated over a column (Sundström et al., 2014). In other words, it tells about how polluted the air is by looking at the attenuation of aerosols in the vertical column. Other parameters, such as fine particulate matter, can further be calculated using satellite measurements of AOD (Van Donkelaar et al., 2010). Satellite data provide regional insights of the aerosol loading on a daily to weekly scale, whereas ground-based instruments have a better resolution.

2.2.1 Health effects of aerosols and air quality index

One of the basic requirements of human well-being and health is clean air, but, unfortunately, air pollutants worldwide threaten the human health (WHO, 2017). In the developed countries in North America and Europe, however, stricter air quality regulations and outsourcing of factories to developing countries have resulted in a decline in aerosol concentrations. On the contrary, in developing countries, rapid urbanization together with industrialization has led to an increase in anthropogenic emissions in the recent decades (NASA, 2010). Especially in Asia, where the amount of anthropogenic emissions has increased in the past decades, the air pollutants contribute to great environmental health risks. It is shown that being exposed to air pollutants, either shortly or for a longer time, increases the mortality rates and hospital visits, and is associated with respiration and cardiovascular diseases (e.g. Brunekreef and Holgate, 2002). Furthermore, in a study, where the health effect of air pollutants in China was compared with health risk factors concerning cigarette smoking, it was shown that outdoor air pollutants also affect the life-expectancy of humans when being exposed to poor air quality. In highly polluted cities, a reduction in life-expectancy of up to 3 years is to be expected, which is a fourth of the estimated reduced years in life-expectancy due to heavy cigarette smoking (Dockery and Pope, 2014). Further highlighted in the study is the fact that smoking is a personal choice, whereas breathing in a city, where the air is highly polluted, exposes the whole population to the polluted air.

There are general agreements how to classify air quality. The Air Quality Index (AQI) has six categories based on limits for the concentrations of fine particulate matter ($PM_{2.5}$) calculated as a 24-h average. Real-time AQI values are published and open for common use (AQICN, 2017). New updates in the $PM_{2.5}$ breakpoints for the AQI conversion scale were made for the Asian cities in order to present air quality standards that are stricter. Since September 2013, all countries are using the same standards for AQI classifications. The categories together with the index values and breakpoints for $PM_{2.5}$ concentrations are shown in Table 1.

The World Health Organization present air quality guidelines (AQG) that are developed to support cities for achieving air qualities of no harm for the public health, i.e. to protect public health. The long-term recommendation in AQG for $PM_{2.5}$ given in terms of annual mean is 10 µg m^{-3}, which is equivalent with a value of 25 µg m^{-3} given as 24-hour average. This value is found within the moderate AQI category (see Table 1). WHO (2017) further highlights the increased risks related when annual or hourly mean concentrations exceed the given AQG value. A 24-hour mean concentration of fine particulate matter of 75 µg m^{-3} leads to 5 % increased risk related to long-term mortality rates, and additionally, more than 15 % higher mortality risk is combined with annual mean concentrations exceeding 35 µg m^{-3}. Van Donkelaar et al. (2010) used measurements of AOD for calculating global long-term fine particulate matter concentrations and using this approach, the annual mean concentrations over eastern China were stated to exceed 80 µg m^{-3}, clearly exceeding the threshold of 35 µg m^{-3} annual average given by WHO. The aerosol concentrations measured in most of the cities in China thus exceed national and international standard values (e.g. Gao et al., 2009).

Table 1. Air quality index (AQI) categories and the representative standards and interval values for the fine particulate matter concentrations for each AQI category (based on AQICN, 2017).

AQI category	Index values	Breakpoints (µg m^{-3}, 24-h. aver.)
Good	0 – 50	0.0 – 12.0
Moderate	51 – 100	12.1 – 35.4
Unhealthy for sensitive groups	101 – 150	35.5 – 55.4
Unhealthy	151 – 200	55.5 – 150.4
Very unhealthy	201 – 300	150.5 – 250.4
Hazardous	301 – 400	250.5 – 350.4
Hazardous	401 – 500	350.5 – 500

2.2.2 Air quality in Beijing, China

Figure 3. The view in Beijing during high air pollution values. The air quality was announced as “apocalyptic” during the capture of this photo. This photo is taken 30.7.2016 by Inka Reinola.

In China, the main sources for emissions are in the east and south, such as Beijing (north-east), Shanghai (east) and other high populated areas (Sundström et al., 2012). Furthermore, degree of urbanization and industrialization has an impact on the fine particulate matter ($PM_{2.5}$) concentrations in China: high concentrations of $PM_{2.5}$ are measured southeast of Beijing in Hebei and Tianjin provinces and further towards southeast, whereas lower concentrations were obtained mostly in western China (Han et al., 2014). The overall air quality index for Beijing is 68 (AQICN, 2017), which lies in the moderate air quality category, with $PM_{2.5}$ values between 12.1 and 35.4 µg m^{-3} (Table 1). This is, however, only the overall index and temporarily the air quality in cities in China can be really poor (see Figure 3). In special conditions, for example during winter when the boundary layer, the atmospheric layer which is in immediate contact with the surface, in urban areas can maintain stable, the atmospheric stratification can restrict the spreading of pollutants (Karsisto et al., 2016; Zheng et al., 2015), which will give space to very hazardous conditions. High aerosol concentrations can furthermore impact the urban boundary layer by increasing the stability and decreasing the boundary layer height, thereby worsen the air quality at the surface (Petäjä et al., 2016). In 2013, AQI values higher than 500 together with extremely high concentrations of fine particulate matter were measured, giving air quality to be categorized as bad as beyond the given index standards (Dockery and Pope, 2014). These severe haze events during winter 2013 in Beijing were additionally shown to be initiated and controlled by regional transport of pollutants, that can sharply increase the aerosol concentrations and thereby impact the variations found in the measured local air pollution concentrations (Zheng et al., 2015).

Additionally, the air quality in Beijing is determined by meteorology in terms of wind, high humidity and air temperature, as well as by topography. In summer, the combination of low wind speeds, high humidity and air temperature values and the surrounding hills in the north can restrict the air flow to be mixed, causing air pollutants to reside for several days before being removed by the wind or rain (Streets et al., 2007). The regional transport of pollutants is therefore important also in summer, when winds from more polluted areas, such as from Hebei province, can be blocked by mountain ranges, causing air pollutants to accumulate in the affected areas (Sundström et al., 2012). The surrounding provinces (Hebei and Tianjin) contributes monthly with up to 30 % of the small particle concentrations measured in Beijing (Streets et al., 2007).

There are, however, improvements made and plans in order to improve the bad air quality. An effort was made during the Olympic games in 2008 in Beijing, having the aim that the athletes and attendees would be able to enjoy the games without having to face the air pollution problems (Liu et al., 2012). Improvements included traffic restrictions for two months (20^{th} of July to 20^{th} of September), prohibition of high-emission vehicles, closing factories and temporarily shutting down of industries in the surrounding regions. The importance of the latter improvement is also highlighted in the study made by Streets et al. (2007). Regional air quality management is emphasized, since pollutants can be transported by the wind to Beijing from nearby sources with less strict pollution control policy, thereby remarkably impacting the air quality in Beijing, also during the Olympic games.

2.2.3 Aerosol direct and indirect effects on the climate

The health issues alone are not the only worrying factor and the reason for concerns when looking at air pollutants. The radiative properties of the aerosol particles are also of great importance (Haywood and Boucher, 2000).

Firstly, the radiative budget of the Earth, is influenced by the atmospheric aerosols directly by scattering and absorbing solar and thermal infrared radiation (Sundström et al., 2014; Haywood and Boucher, 2000). Whether the aerosol direct radiative effects are cooling or warming depend on e.g. aerosol optical properties, type of aerosol, properties of Earth's surface and the particle concentration (Sundström et al., 2014). Furthermore, in a study of how an aerosol layer affects the temperature profile on urban environments it is found that the relation between solar and infrared absorption determines the net effect the polluted layer has on the temperature change due to their radiative effects (Atwater, 1971). When pollutants are present, they both increase the downward infrared radiation flux to the surface as well as reflect and absorb the incoming solar radiation. During the night, with lack of sunlight, the aerosols mostly increase the surface temperature due to the re-emission of longwave radiation towards the surface. The daytime surface cooling due to the reduction in incoming solar can be compensated by the surface warming due to enhanced downwelling longwave radiation caused by urban aerosols during nights (Nair et al., 2011).

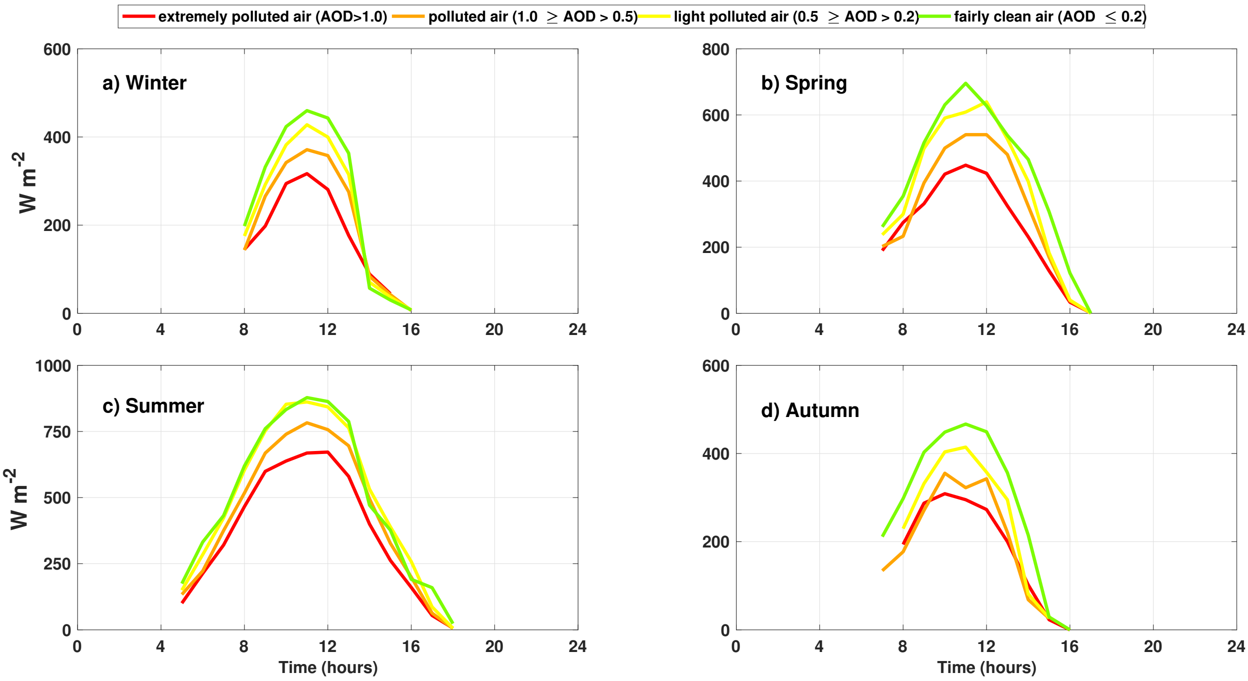

Figure 4. Observed diurnal cycles shown in thermal seasons for downward shortwave radiation ($K\downarrow$), selecting only observations taken when Aerosol Optical Depth (AOD) data is available. The data is further divided into the different pollution categories, indicating the aerosol radiative effect. More details are given in Chapter 2.

Figure 4 illustrates how the incoming solar radiation ($K\downarrow$) is attenuated due to presence of aerosols in Beijing, shown in four pollution categories according to measured AOD values. During clean air conditions, the maximum absolute value for $K\downarrow$ in the different thermal seasons are: 460, 696, 878 and 467 W m^{-2}, showing the highest values obtained in summer, as expected. The similar values during extremely polluted air conditions are following: 317, 448, 672 and 309 W m^{-2}. The highest difference between these two extreme conditions occur in spring, accounting for 248 W m^{-2}, whereas the other differences are smaller, but still noticeable: 143, 206 and 158 W m^{-2} for thermal winter, summer and autumn, respectively.

Secondly, the aerosols affect the climate also indirectly by acting as cloud condensation nuclei

(CCN) and thereby changing and affecting cloud characteristics and radiative properties (Lamb and Verlinde, 2011; Haywood and Boucher, 2000), such as cloud albedo (=capability of reflecting shortwave radiation) and emissivity (=capability of radiating longwave radiation). When the air is polluted, the excess water vapor in the air will be quickly consumed by the aerosols, resulting in many small cloud droplets, compared to clean air situations, when the formed droplets can continue to grow due to less particles available in sharing the excess water vapour (Lamb and Verlinde, 2011). Therefore, in clean marine boundary layers the aerosol concentrations are smaller and maritime clouds have low concentrations of CCN in comparison to continental clouds due to higher aerosol concentrations in the continental boundary layer.

The concentration of CCN in the cloud has a huge effect on both cloud radiative properties, referred as “cloud albedo effect”, and cloud lifetime and precipitation rates, referred as “cloud lifetime effect” (e.g. Haywood and Boucher, 2000). Firstly, smaller cloud droplets, due to higher concentrations of pollutants in the air, increase the ability of clouds to scatter the incoming solar radiation. This albedo effect reduces the net solar energy reaching the surface and has therefore a cooling influence on the climate (Lamb and Verlinde, 2011). Due to the seasonality of shortwave radiation, an increase in aerosols could alternatively oppose the cooling effect by influencing the longwave emissivity of thin clouds. Larger amount of smaller cloud droplets can make thin clouds to be opaquer, trapping more heat and re-emitting more thermal energy to the surface (Garrett et al., 2002). Secondly, larger droplets can grow faster, leading to effective precipitation followed by dryer air and diminishing of the resisting cloud (Lamb and Verlinde, 2011). As a conclusion, longer lifetime, increased cloud cover and decreased precipitation efficiency are expected of clouds with a high concentration of small droplets, being able to affect the radiation for a longer time.

As a summary, aerosols are important particles in the air due to their influence on both the environment and human health, as well as the important role they have on the global climate due to aerosol radiative properties, both directly and indirectly via clouds.

3 Data and Methods

3.1 Model description

The model used in this study is the Surface Urban Energy and Water Balance Scheme (SUEWS, Järvi et al., 2014, 2011; Ward et al., 2016) that can simulate the surface energy and water balances in urban areas using only commonly measured meteorological values and information on surface cover characteristics. The hourly meteorological forcing data provided for the model include incoming shortwave radiation ($K \downarrow$), air temperature (T_{air}), humidity and wind speed (Table 4). In simulations, extended version (SUEWS_V2015a) of the published model version SUEWS_V2014a (Järvi et al., 2011) with improved model parameters for the surface conductance (Ward et al., 2016) is used. SUEWS is a rather simple model and does not need any high-tech computers to enable running the model, which is one of the key advantages of SUEWS (Ward et al., 2016).

SUEWS is centred on the surface urban energy balance (Oke, 1987) utilizing the evaporation-interception approach (Grimmond and Oke, 1991). It also includes components from the urban water balance model that was the first urban water model using actual evaporation rates and used with a time step of one day (Grimmond et al., 1986). SUEWS provides information on every time step for each component in the radiation and energy balance equations (2.2 and 2.3), as well as surface soil wetness information for each surface type together with surface and soil runoff (Ward et al., 2015). The different model input and output variables can be seen in Table 4 and Table 5. Different versions of SUEWS has been evaluated mainly in high- and mid-latitudes, such as in Los Angeles and Vancouver (Järvi et al., 2011), in the UK (Ward et al., 2016) and in Singapore (Demuzere et al., 2017). There is, however, a lack of information from countries and cities in Asia.

In SUEWS the simulated area is divided into seven surface types: non-vegetated areas (paved, buildings and bare soil), vegetated areas (evergreen trees/shrubs, deciduous trees/shrubs and grass) and water (rivers, lakes, pools and fountains). The vegetated areas can be irrigated and the proportions individually for grass surfaces, evergreen and deciduous trees, shall be specified (Ward et al., 2015). The model calculates the soil moisture, using the evaporation-interception approach, and surface soil state for every different surface type at each time step separately, both for the surface types on the single surface layer as well as for the single soil layer below each surface type, except for water. Horizontal water movements are also considered (Ward et al., 2015).

SUEWS includes several sub-models in order to minimize the required number of input variables for simulating the different components of the SEB. The Net All-wave Radiation Parameterization Scheme (NARP; Loridan et al., 2011) is used for calculating the net all wave radiation (Q^*), Objective Hysteresis Model (OHM; Grimmond et al., 1991; Grimmond and Oke, 2002) for calculating the storage heat flux (ΔQ_S)

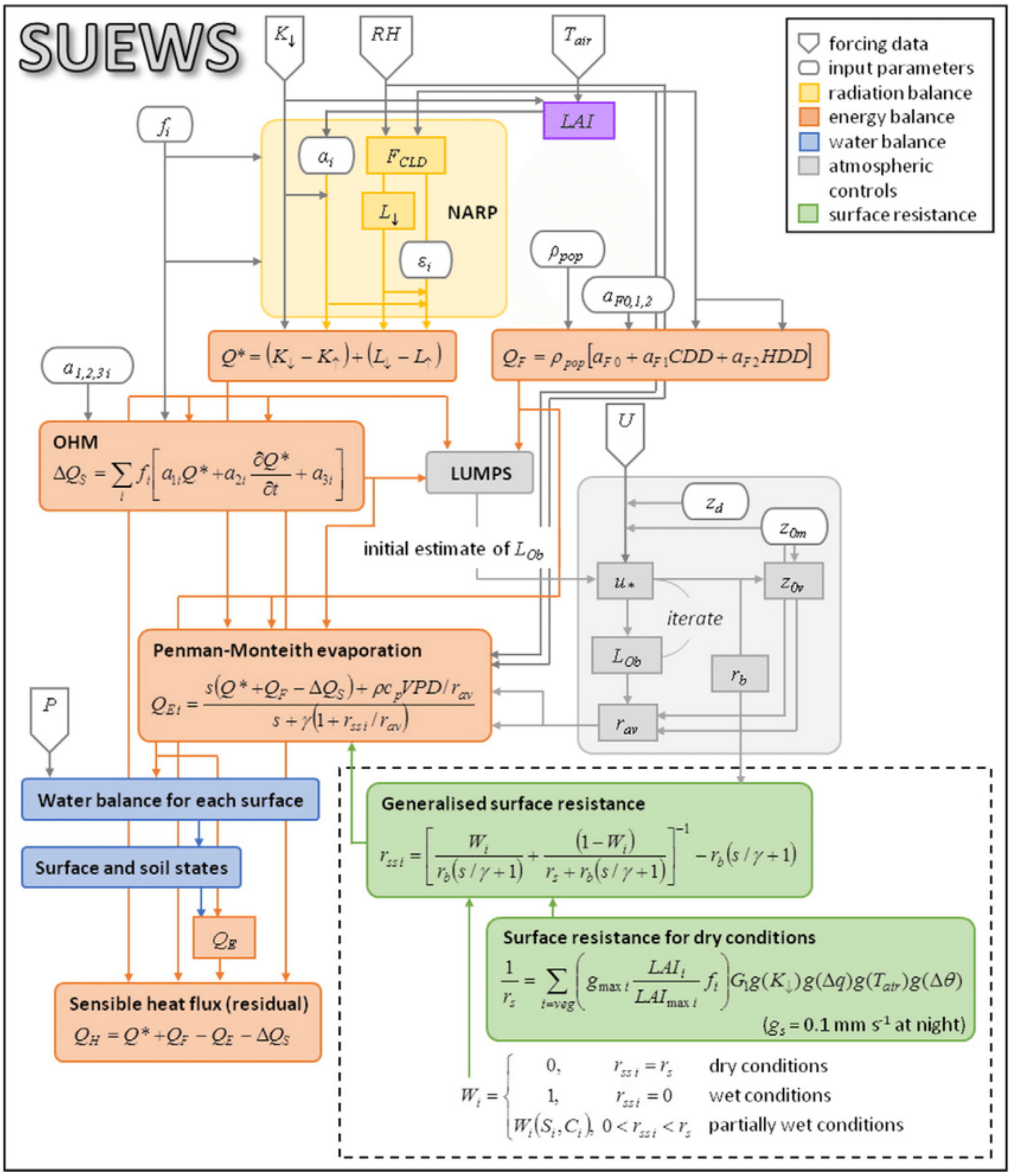

Figure 5. Overview of the key processes in SUEWS, including all the general parameters as well as the meteorological forcing data required for the model run (Ward et al., 2016). Further details can be found in (Järvi et al., 2011) and SUEWS manuals (Ward et al., 2015).

and the Local-scale Urban Meteorological Parameterization Scheme (LUMPS; Grimmond and Oke, 2002) provides initial calculations for the atmospheric stability, needed for estimations for the turbulent heat fluxes (Q_E and Q_H). Furthermore, the anthropogenic heat flux (Q_F) is calculated using a simple model, where the determined population density and heating and cooling degree days (HDD and CDD) act as inputs in the estimation of Q_F (Järvi et al., 2011). The daily Q_F is calculated separately for weekdays (wd) and weekends (we) and defined per population density. The anthropogenic moisture emissions are not included in the model calculations. Q_E is calculated using the Penman-Monteith equation that is modified especially for urban areas (Grimmond and Oke, 1991). Through this evaporation-interception scheme, where the available water on the surface changes due to rainfall or irrigation, realistic hourly estimates for the latent heat flux as well as the average water state is being provided. Q_H is calculated as a residual term from Equation 2.3. Figure 5 illustrates the main functions of SUEWS and how the sub-models inside the model work, combined with the required model parameters (see Appendix B for notation explanations).

3.2 Study area

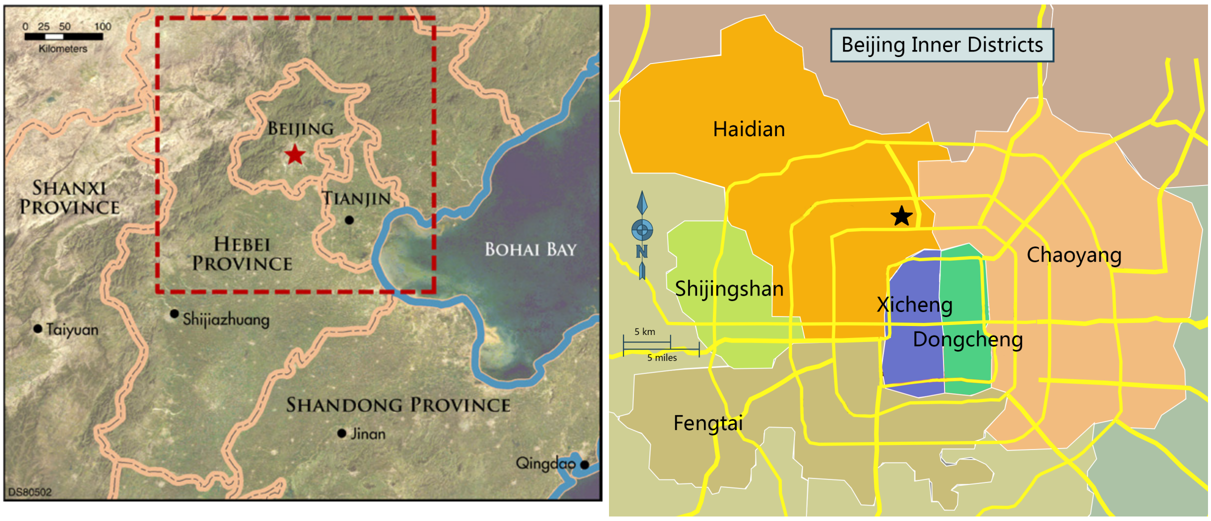
(a)

(b)

Figure 6. **a)** Map over Beijing and the surrounding areas, including the Hebei and Tianjin Provinces. The red square indicates 4 km model domain used in the study of Streets et al. (2007). **b)** Map showing the inner districts from the 16 districts belonging to the Beijing Municipality. The approximate location of the meteorological tower is marked on the map with a star. The ring roads centring the city is also shown on the map (modified from Wikivoyage, 2010).

Beijing is the capital of the Republic of China located in northern part of China (Figure 6) and is the second largest city after Shanghai with a population of over 20 million people. The city is surrounded by mountains in the north and west whereas the northern part of the North China Plain extends to the southern and eastern parts of the city. The city is build up from concentric ring roads. The city belongs to a monsoon influenced humid continental climate, with humid and hot summers by the influence of the East Asian monsoon. The winters, in contrary, are mostly dry and cold due to the influence of the Siberian anticyclone.

The SUEWS model is run for the study area of a 1 km radius circle around the Beijing meteorological tower (39° 58′ N, 116° 22′ E), located in the north-western part of the city (Liu et al., 2012). The tower is in the Haidian district, but the chosen source area of 1 km radius circle around the tower contains areas also belonging to the nearby Chaoyang and Xicheng districts (see Figure 6 and Figure 7). Required site specific variables for the model run include surface cover fractions of the plan area, population information, mean building and tree heights for each surface type and some hydrological input data as initial condition information. The site-specific parameters as well as defined initial conditions for the study area are provided in Table 2. The building height (25 m) is determined based on values presented in (Song et al., 2013) and the tree height (8 m) based on the heights of the most common trees reported to be grown in Beijing (Ma et al., 2003). The starting and ending day of irrigation were assumed based on that no irrigation occurs during winter months (December−February).

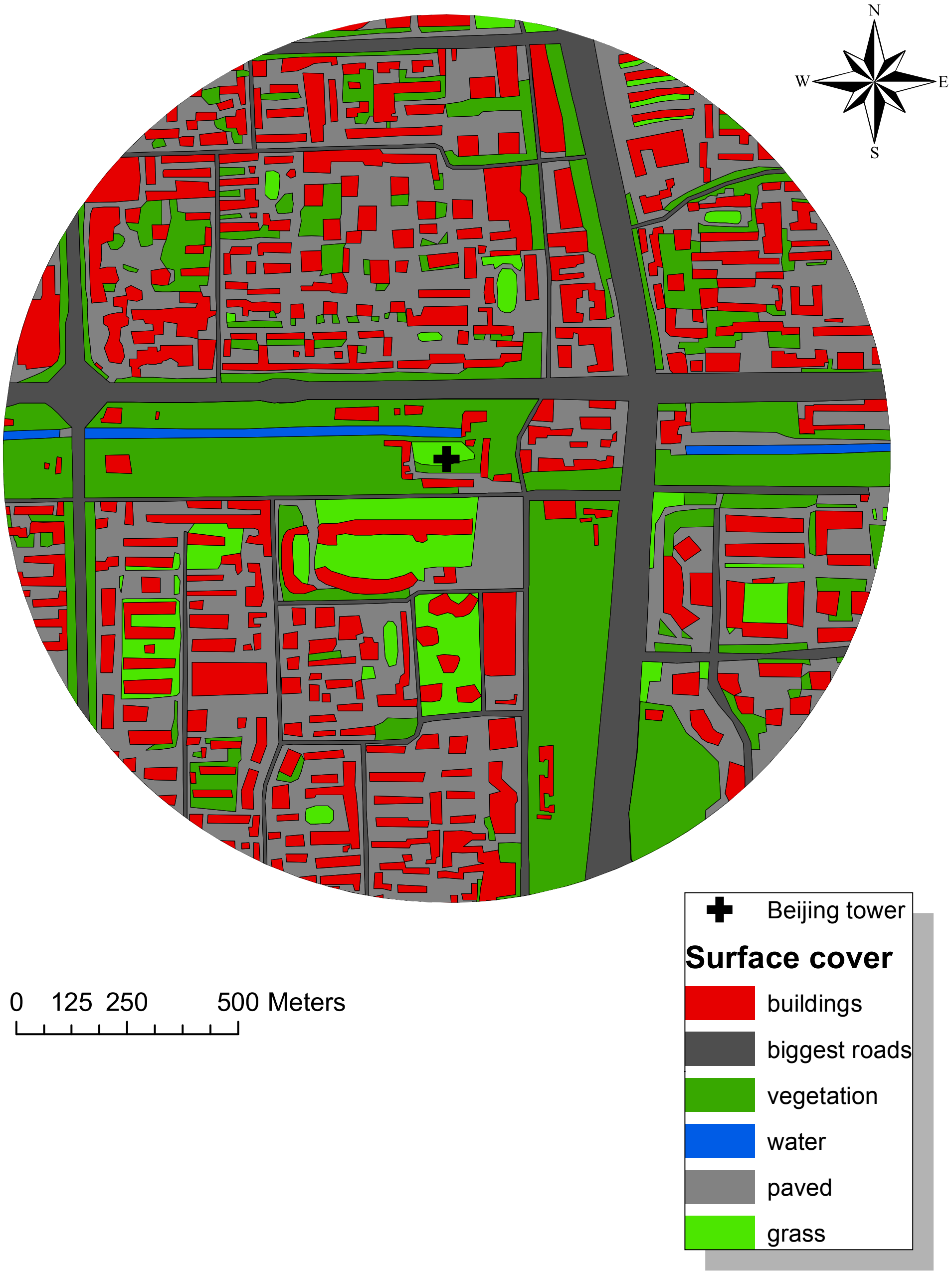

Figure 7. Digitalized surface covers for the study area of 1 km radius circle around the Beijing tower that is marked as a plus on the map.

The four surface cover fractions for the study area are determined from aerial photographs using ArcGIS 10.1, a geographic information system (GIS) used for creating and analyzing maps and mapped information (Esri Inc, 2015). The surface cover fractions were digitalized (Figure 7) using two freely available base maps: OpenStreetMap and Word Imagery. With the available imagery, separating the vegetated tree areas into evergreen and deciduous trees and shrubs needed by the model is not possible. These fractions are based on the common tree species to be found in Haidian district (Ma et al., 2003). The final defined surface cover fractions are listed in Table 2.

Table 2. Site specific parameters and initial conditions for the simulated area. See text for more information about how the variables were determined for the study area.

Parameter [abbr.]	**Unit**	**Value**
Year	–	2006 – 2009
Latitude [lat]	°	39.97
Longitude [lon]	°	-116.37
Timezone [T_{zone}]	UTC	8
Model time step[T_{step}]	s	300 (5 min)
Height above ground [z_m] (measurement height)	m	47.0
Model surface area [A]	ha	314.16
Altitude, Mean topographic height above sea-level	m	48.63
Mean tree height (both evergreen and deciduous) [z_t]	m	8
Mean building height [z_h]	m	25
Roughness length of momentum [z_0]	m	RT*
Zero-plane displacement [z_d]	m	RT*
Surface cover fraction of paved surfaces	–	**0.47**
Surface cover fraction of buildings	–	**0.24**
Surface cover fraction of evergreen trees and shrubs	–	**0.17**
Surface cover fraction of deciduous trees and shrubs	–	**0.01**
Surface cover fraction of grass	–	**0.1**
Surface cover fraction of bare soil or unmanaged land	–	**0**
Surface cover fraction of open water	–	**0.01**
Fraction of evergreen and deciduous trees that are irrigated	–	0.31
Fraction of grass that is irrigated	–	0.70
Population density (mean for the study period)	pop ha^{-1}	76.5
Starting day for irrigation	DOY	60**
Ending day for irrigation	DOY	334**

*calculated inside the model using mean building height and tree height according to the "Rule of Thumb" method described by Grimmond and Oke (1999a).
**In the model run, assumptions were made that no irrigation occur during winter months (December−February).

Table 2 continues.

Parameter	**Unit**	**Value**
Initial conditions		
Days since precipitation	d	29
Previous day mean temperature	°C	-4.1
Evergreen tree albedo on day 0 of the run	–	0.10
Deciduous tree albedo on day 0 of the run	–	0.12
Grass albedo on day 0 of the run	–	0.18
Deciduous storage capacity on day 0 of the run	mm	0.3
Porosity on day 0 of the run	–	0.2
Surface water states (wetness state)	mm	0
Initial state of the soil water storage under paved surfaces	mm	70
Initial state of the soil water storage under buildings	mm	30
Initial state of the soil water storage under vegetated surfaces	mm	130

The heterogeneous surroundings, with both parks and green areas together with buildings, roads and highways and a small river flowing north of the tower, are due to the fast urbanization in Beijing since 1980s. The area is completely different nowadays compared to year 1979 when the meteorological tower was built and when it was surrounded by rural areas and low built houses (Liu et al., 2012). The Beijing-Tibet Expressway east of the tower and another busy road north of the tower, Beitucheng Road, contribute with heavy traffic loads. Residential areas are located both to the south and north of the tower, with tallest buildings in the southwest. The vegetation cover is also decreased in these residential areas.

For the study period of 2006−2009, population densities in the study area for each year were calculated as a weighted mean from the three districts that coincide with the study area (City Population, 2014). The calculations were made based on the population growth rates and the population density in year 2000 given for each district and the areal fractions of each district estimated for the study area (Table 3). For the study area, the population density for year 2000 was estimated from the densities given for each district and weighted by their areal fractions. The calculated population density growth rate for the study area was then applied for calculating the final estimated population densities valid for the study area for the study period 2006−2009. The values in the last column from Table 3 are used as final population densities for the study area.

Table 3. Population densities and areal fractions for the three districts that coincide within the study area. The final weighted mean density estimated for the study area is shown in the last column. The population densities for 2000 as well as the growth rate are taken based on values provided in City Population (2014). See text for detailed explanation.

	Haidian	Chaoyang	Xicheng	Study area
Area (ha)	43100	45500	5100	314
Population (2000)	2 240 124	2 289 756	1 232 823	–
Population density growth*	+3.89%	+4.47%	+0.08%	+3.39%
Population density in 2000 (ha^{-1})	52	50	242	57
NumCapita (ha^{-1}) for 2006	65	65	243	72
NumCapita (ha^{-1}) for 2007	68	68	243	75
NumCapita (ha^{-1}) for 2008	71	71	244	78
NumCapita (ha^{-1}) for 2009	73	74	244	81
Areal fractions of the 1 km radius circle (%)	70	27	3	100

*per year between 2000−2010.

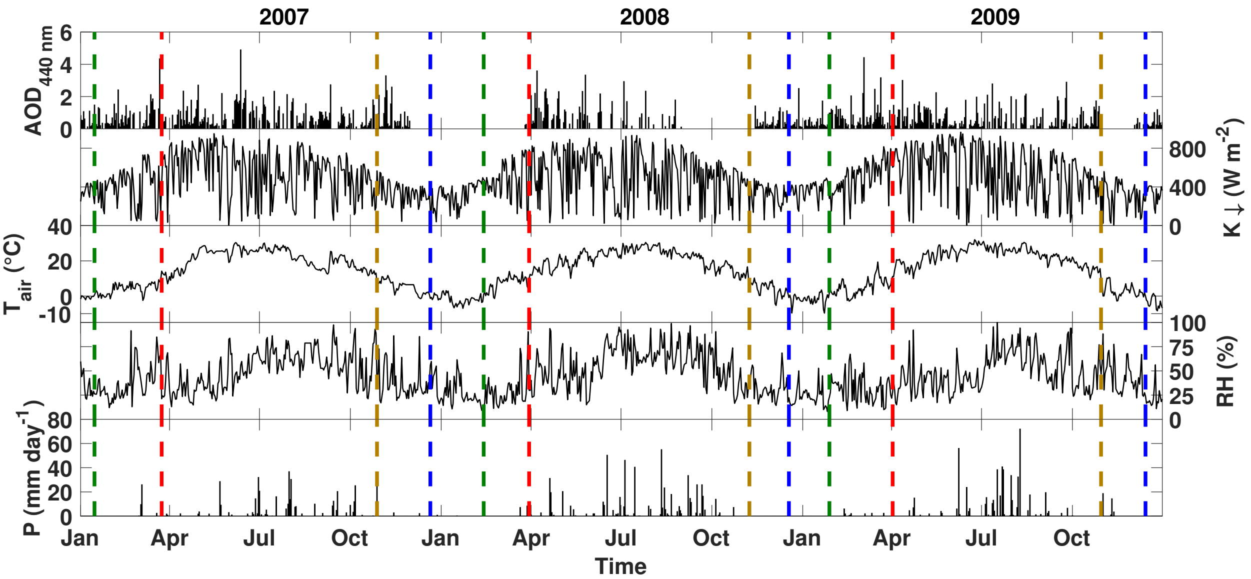

Figure 8. Time series of daily values calculated for four measured meteorological variables: incoming shortwave radiation ($K\downarrow$), air temperature (T_{air}), relative humidity (RH) and precipitation (P), as well as aerosol optical depth (AOD) measured at the wavelength of 440 nm. The $K\downarrow$ is calculated using observations around noon, between 10−14. The vertical lines indicate the starting day of the thermal seasons, where green indicates the start of spring, red start of summer, brown start of autumn and blue start of winter, respectively. See Section 3.5 for more details concerning the definitions of the seasons.

The general weather conditions in Beijing during the study period are shown with a climate diagram in Figure 9, whereas Figure 8 shows time series of meteorological data observed from the study area. The five timeseries include daily precipitation, relative humidity, daily air temperature and incoming shortwave radiation, as well as daily aerosol optical depth (AOD)-values measured at the wavelength of 440 nm (see Section 3.4). There is a clear difference between the precipitation observed during summer compared to the low values in winter, as well as large seasonal variations in air temperature. Separation between a dry and a wet period can be made, where the wet period occurs from May to October (Liu et al., 2012).

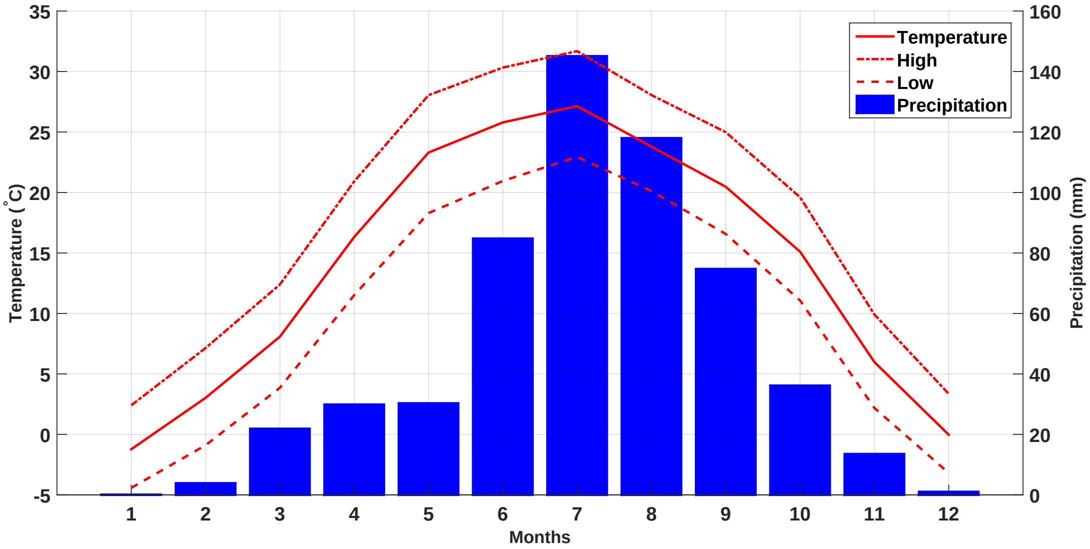

Figure 9. Climate diagram based on the observed meteorological data from the study period (2007−2009). The mean values for the maximum and minimum temperatures each month is also shown on the diagram.

The climate in Beijing and the dry/wet period is influenced by the East Asian summer and winter monsoon. The more familiar term indicating this period of heavy rainfall, concentrated in South Asia, is referred as “Asian Summer monsoon” (Chang, 2004). The “East Asian summer Monsoon”, on the other hand, is characterized by a more complex structure in both space and time, consisting of alternating and more concentrated elongated rain belts, which makes these areas more sensitive to inter-annual variations due to the complex structure and propagation of the rain belts. In fact, the Asian summer monsoon starts to break out in mid-May, causing a pre-summer rainy season over South Asia, after which it suddenly finds two different routes: one propagating towards India and the second one travelling towards north- and northeast, finally extending to North China one month later, in mid-June (Chang, 2004). This penetration of the monsoon rains is also visible in the data from Beijing, where a sudden increase in the monthly precipitation between May and July is noticeable (Figure 9). The mean annual total precipitation received in Beijing based on the data observed during the 3-year study period was 560 mm, with 451 mm measured in 2007, 621 mm in 2008 and 605 mm in 2009, respectively. The wettest month according to Figure 9 is July, when in 2009 the observed precipitation was 224 mm. In 2008, the rainiest month was exceptionally in September (138 mm). The daily maximum precipitation over the whole study period was measured on the 9^{th} of August 2009. The last timeserie shown in Figure 8 illustrates daily rain events and the observed amounts.

The coldest day during the study period occurred in December the 21^{st} in year 2008 with daily mean air temperature of -12.4 °C and warmest day (39.3 °C) was in 2009 in June the 24^{th} with hourly temperatures over 45 °C (Figure 9). The average daily air temperature during the 3-year period was 14.0 °C. The seasonal monsoon alters the wind fields, leading to southerly wind direction during summer and the opposite in winter. Liu et al. (2012) also showed that the prevailing wind directions in Beijing are northwest and southeast, where higher wind speeds are observed more often during northerly winds compared to the southerly winds. This was mainly affected by the tall urban buildings located in the south of the study area.

3.2.1 Measurements

From the required meteorological forcing data, air temperature, relative humidity and wind speed are measured at 47 m above ground level at the 325-m high Beijing tower located in the middle of the study area (Figure 7). Solar radiation ($K\downarrow$) is measured from a nearby roof at the same height, whereas the daily surface pressure and precipitation are obtained 10 km southeast of the tower at Caoyang weather station. Due to the input data resolution of one hour, the daily pressure is considered to maintain the same throughout the whole day and precipitation is divided arbitrary for the each hour in a day depending on its intensity and magnitude.

To value the model performance, eddy covariance (EC) observations of the turbulent sensible and latent fluxes (Q_H and Q_E) measured also at the height of 47 meters of the Beijing meteorological tower are used (Liu et al., 2012; Song et al., 2013). The EC system includes a 3D ultra sonic anemometer (CSAT3, Campbell Scientific, 2017) and an open-path infrared gas analyzer (LI-7500, Licor Inc, 2017), both with sampling frequency of 10 Hz. The first is a precise instrument to measure directly all three wind components and the sonic temperature whereas the second measures water vapor fluctuations and CO_2 concentrations. Daily and hourly data coverage of the turbulent fluxes is provided in Appendix C. Figure 10 also shows the diurnal distribution of missing data from these turbulent measurements and AOD-data, presented in thermal seasons (see Section 3.5).

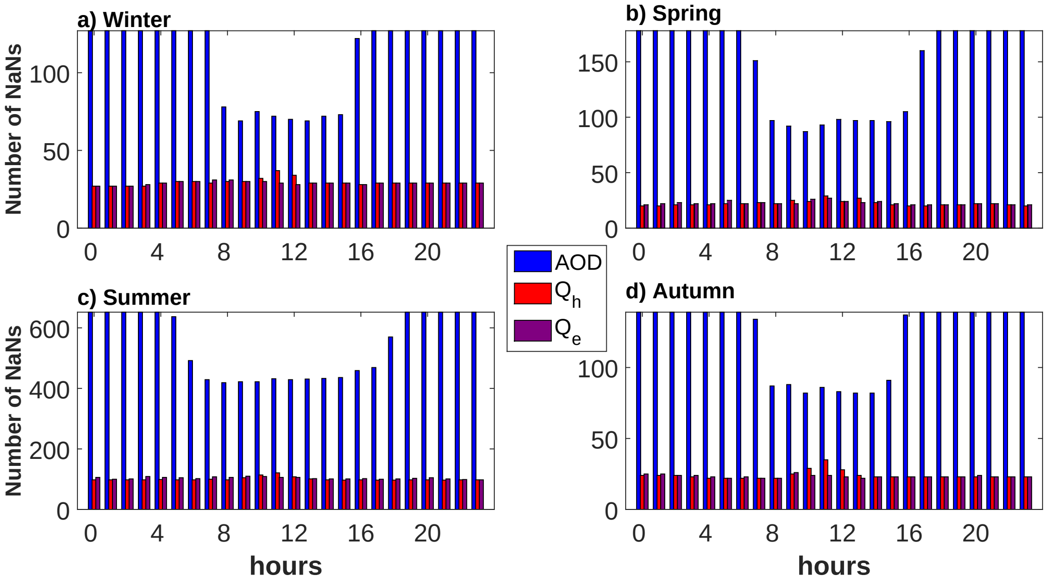

Figure 10. Diurnal amount of missing data of Aerosol Optical Depth (AOD) (blue), Q_H (red) and Q_E (purple) during different thermal seasons. Detailed information about the seasons and AOD is given in the next chapters. Total amount of days for the study period of three years are 124 days for winter, 178 days for spring, 652 days for summer and 142 days for the winter season.

3.3 Model run

For the model to run, also common site-specific parameters for each surface type are specified, emphasizing conditions valid for this study area. The specified characteristics include albedo, emissivity, moisture storage capacity and drainage coefficients for each surface type (Appendix A). For the vegetated surfaces, additional vegetation characteristics are required (for example leaf area index (LAI), extreme values), as well as drainage and soil characteristics.

The parameters used in this model run are mostly default parameters, based on the values from Järvi et al. (2011) if not otherwise mentioned. Notably, the model run takes advantage of an alternative parametrization for the surface conductance (Ward et al., 2016). The main difference here to the previous model version is that larger soil moisture deficits are allowed before limiting the evaporation from non-irrigated surfaces. In calculating the storage heat flux, the OHM-coefficients for the different surfaces (e.g. paved) are calculated as an average from coefficients given for concrete and asphalt surfaces. Due to no additional input data concerning the radiative components, the $L\downarrow$ is calculated from the given air temperature and relative humidity.

The model is using one year (2006) as spin-up time, which purpose is to remove model's dependency on the initial values chosen by the user. The rest of the period, 2007−2009, is used for analysis and model evaluation. The model is run with 5 min time step and the output is averaged back to 60 min resolution of the forcing data. These linear conversions made inside the model for the required forcing data to and from 5 min time steps result in differences seen between the hourly input and output data of $K\downarrow$ (Ward et al., 2016). In data analysis, the meteorological forcing data is used for T_{air} and $K\downarrow$ due to the model modifications on these values. An overview of the parameters used in the model can be found in Appendix A (see Appendix B for further notations). Table 4 (5) list the model input (output) variables.

Table 4. Input variables and meteorological data required for the model run. Additional optional input variables can also be specified (if available), but in this model run only the required meteorological input variables were given as forcing data to the model.

Variable	**Units**	**Variable**	**Units**
year (*iy*)	YYYY	Relative humidity (*RH*)	%
Day of year (*id*)	DOY	Air temperature (T_{air})	°C
Minute (*imin*)	M	Station air pressure (*pres*)	kPa
Hour (*it*)	H	Incoming shortwave radiation ($K\downarrow$)	W m^{-2}
Mean wind speed (U)	m s^{-1}	Precipitation (P)	mm

Table 5. Selected output variables provided by the model. From the output variables, only the ones related to SEB are used.

Variable	**Units**	**Variable**	**Units**
Net all-wave radiation (Q^*)	W m^{-2}	State of the surface*	mm
Radiation components ($K\uparrow, L\downarrow, L\uparrow$)	W m^{-2}	Change in surface and soil stores	mm
Surface temperature (T_{surf})	°C	Runoff (R)**	mm
Sensible heat flux- LUMPS/SUEWS (Q_E)	W m^{-2}	Soil runoff (in the subsurface)	mm
Latent heat flux- LUMPS/SUEWS (Q_H)	W m^{-2}	Internal water use***	mm
Storage heat flux (ΔQ_S)	W m^{-2}	Aerodynamic resistance (*ra*)	s m^{-1}
Anthropogenic heat flux (Q_F)	W m^{-2}	Surface resistance (*rs*)	s m^{-1}
External water use in the study area (I_E)	mm	Friction velocity (u^*)	s m^{-1}
Evaporation (E)	mm	Obukhov length (L)	m
Drainage (D)	mm	Soil moisture	mm
Leaf area index (LAI)	m^2 m^{-2}		

* separately for the different surface types.

** separated in above ground runoff (on paved and vegetation surfaces) and runoff received from pipes.

*** separated for irrigation of the different vegetation surfaces.

3.4 Aerosol optical depth

In order to understand the aerosol impact on the SEB, it is vital to obtain accurate information about aerosol optical properties and concentrations. AERONET (AErosol RObotic NETwork) is a ground-based remote sensing network of instruments, operated in scales from local to global and designated for monitoring aerosols. It was established by NASA and works today as a data archive for characterizing aerosols, such as optical, microphysical and radiative properties (Holben et al., 1998). Developments made on the AERONET instruments, such as on spectral radiometers that can automatically scan the sun and sky, provide data about aerosol optical properties in a relative frequent pace. These sun-sky scanning radiometers are also called sun photometers. The observations for this study are obtained from an automatic CIMEL sun photometer that can make direct sun measurements in eight different bands between wavelengths of 440 nm and 1020 nm. To identify haze in Beijing, total column AOD measurements at 440 nm and 1020 nm recorded by the AERONET station located in Beijing (39.97689 N 116.38137 E) is used. For this study, we mostly use data collected at the wavelength of 440 nm, because this wavelength is more sensitive to smaller particles than AOD data at 1020 nm. The data include measurements for the whole study period (2007−2009), taken daily many times within an hour, from which hourly median and daily median values are calculated (top in Figure 8). Due to the need of direct sunlight in the measurement technique for obtaining AOD, there is no data available for the night time as well as in case of cloudy skies and/or precipitation events. Figure 10 illustrates well how the measurements of AOD is dependent on sunlight. AOD data is missing during the time when no sunlight is present, i.e. during nights but also during rainy events or cloudy skies. The relatively high amount of missing AOD values during summer is mainly due to the humid climate and partly cloudy summers in Beijing, where the cloud cover inhibits the direct sunlight and therefore restricts AOD observations. See Table 13 in Appendix C for absolute values concerning the coverage of AOD data.

3.4.1 Pollution categories

The hourly and daily AOD data are divided into different AOD groups to indicate different air qualities (Table 6).

Table 6. Defined pollution categories based on the AOD-data.

Category	AOD-range	Description
1	AOD > 1.0	extremely polluted air
2	$0.5 <$ AOD ≤ 1.0	polluted air
3	$0.2 \leq$ AOD < 0.5	light polluted air
4	AOD ≤ 0.2	fairly clean air

By assigning the AOD values into these four categories and further distinguish with the days related to the different AOD groups, it enables to separate the data into days (or hours) with either polluted or clean air conditions. Table 7 shows the absolute values of how much of the data is divided between each pollution category. Notably is that only 16,4 % of the total data is applicable when concentrating on analysis based on hourly pollution investigations. This low percentage compared to daily AOD data (54 %) is due to the sunlight-dependency of the AOD measurement technique mentioned earlier, resulting in days of missing AOD.

Table 7. Absolute values of hourly and daily data points of available AOD data for the study period of 3 years. The value in the bracket for each pollution category indicates their relative share in percentage of the total available AOD data, whereas the values indicated with a star (*) refer to the percentage of the days/hours corresponding to the whole study period.

Category	**Total days (2007-2009)**	**Total hours (2007-2009)**
1	160 (27)	1033 (24)
2	143 (24)	968 (22)
3	167 (28)	1361 (32)
4	121 (21)	952 (22)
all AOD data	591 (**54***)	4314 (**16.4***)
Total	1096	26304

3.5 Thermal seasons

Even though climatically a more representative way of presenting and analyzing data in Beijing would be using dry and wet periods, in this study it is more useful to look at the data divided into thermal seasons. The main reason is due to the study focus in AOD, which varies strongly with air temperature.

The division into thermal seasons is based on the definitions provided by the Finnish Meteorological Institute (FMI, 2017). The thermal criteria when distinguishing the seasons is defined by the daily mean temperatures (T_{air}) at 0 °C and 10 °C, which allows the lengths of the seasons to differ when comparing serial years. Days when T_{air} is below zero degrees indicates thermal winter, when T_{air} exceeds 0 °C but lies below 10 °C, it is defined as thermal spring. Likewise, thermal summer occurs when the T_{air} is above 10 °C and thermal autumn starts when T_{air} starts to fall again below 10 °C. This can also be noticed in the middle time series of T_{air} in Figure 8. The transition between two subsequent seasons is calculated using cumulative sums of the daily mean temperature and ($T_{air}-$ 10 °C), where the peaks of maximum and minimum values of their cumulative sums indicates the transition phases. For instance, the starting day of the thermal spring can be found at the day, where the minimum value of the cumulative T_{air} is reached. After reaching the minimum value, the T_{air} is over zero degrees. Likewise, the end of thermal spring and start of thermal summer is at the minimum value of the cumulative sum of ($T_{air} - 10$ °C), after which T_{air} is above 10 °C. Figure 11 illustrates how the calculations were done.

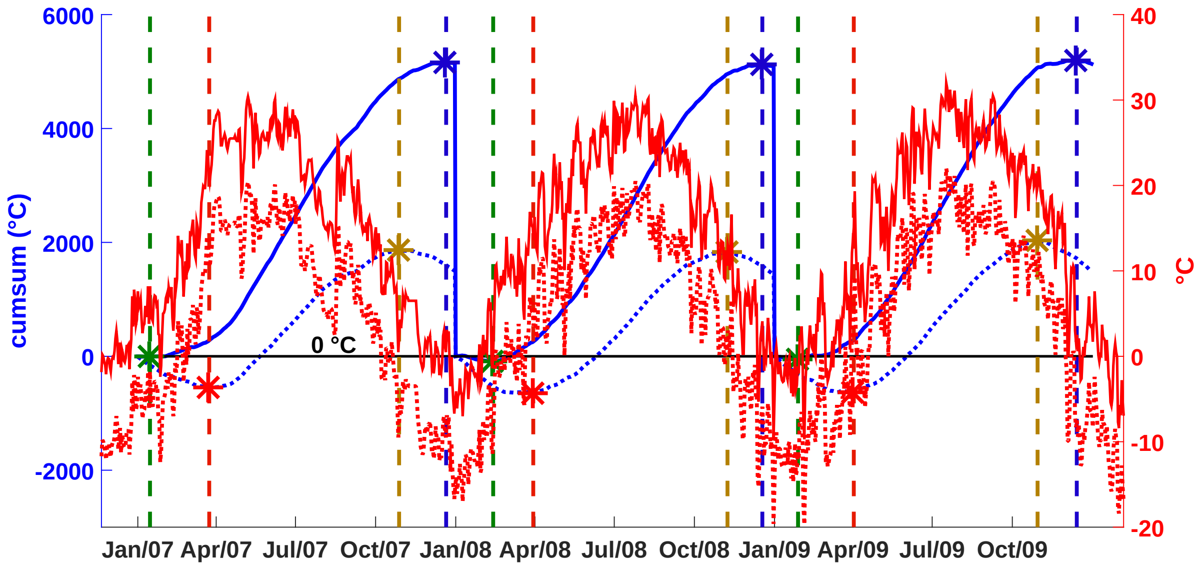

Figure 11. Illustration about how to distinguish seasons using thermal criteria provided by the FMI (2017). The blue line indicates the cumulative sums of daily mean temperature (T_{air}) and the green line for ($T_{air} - 10$ °C) that are also drawn on the figure in red. The vertical lines indicate the final calculated transition phases between the different thermal seasons. The peaks of the cumulative sums are marked with stars, shown in each color of the thermal seasons.

Table 8. Absolute and relative values of hourly and daily data points available each year of the study period and the total sum of the three-year period, divided into thermal seasons. The values in the brackets indicate the relative values of the total in percentage. Additional information about days in each thermal season when AOD data is available is shown in the last column, where the (*) indicates the relative share in percentage compared to total days in each thermal season, separately. More detailed information e.g. in each pollution category can be found in Appendix C.

Thermal season	Days in 2007	Hours in 2007	Days in 2008	Hours in 2008	Days in 2009	Hours in 2009	Total days 07-09	Total hours 07-09	AOD data per day
Winter	25 (7)	600	57 (16)	1320	45 (12)	1056	127 (12)	3048	64 (50*)
Spring	68 (18)	1632	46 (12)	1104	64 (18)	1536	178 (16)	4272	105 (59*)
Summer	218 (60)	5232	223 (61)	5352	211 (58)	5064	652 (59)	15648	356 (55*)
Autumn	54 (15)	1296	40 (11)	1008	45 (12)	1104	139 (13)	3336	66 (47*)
Total	365	8760	366	8784	365	8760	1096	26304	591 (54)

Table 8 presents additional information about the division into thermal seasons. The longest season is summer (60 % of the days) and the others are considerably shorter. The summer periods extend from 24 March to 27 October, 30 March to 7 November and 2 April to 29 October for the three study years of 2007−2009.

The winter periods result in only 12 % of the total days, extending from the end of or mid-December to 14 January 2007, 12 February 2008 and 27 January 2009, whereas spring (15 January−23 March, 13 February−29 March and 28 January−1 April) and autumn (28 October−20 December, 8 November−17 December and 30 October−13 December) covered for 16 % and 13 % of the total days, respectively. Additionally, AOD-data are obtained from half of the days during thermal winter, slightly a smaller amount (47 %) is maintained in autumn, whereas over half of the days in both spring and summer have AOD-data.

In case of data analysis based on dry and wet/rainy periods, the partition of the year in dry (November−April) and rainy (May−October) seasons is made based on Liu et al. (2012).

3.6 Statistics for model evaluation

Models are created among other to predict different phenomena. Because they are only models, errors will occur when doing these predictions, which highlights the need of assessing these errors statistically and being aware of them. There are different ways of evaluating model performance. In this study, scatter plots as well as diurnal figures showing both observed and model predicted values visualize these errors and are supported with statistical parameters. Linear regression is used to find a polynomial fit of first grade, so that the distance between the data points in the scatter plot and the fitted line is as small as possible. The model performance is obviously the better the smaller the differences, also known as residuals, are between observed and modelled values.

Statistical measures presented in this study are R-squared, Root-Mean-Square-Error (RMSE) and Mean-Absolute-Error (MAE). R-squared (R^2) is also known as the coefficient of determination and tells roughly about how close the data points are to the fitted line, i.e. tells about how good the regression line is as an approximation of the location for the real data points. Usually it is presented as percentage and the higher values the better the fit. This is, however, not always the truth, and under certain conditions low R^2 values can be given even though a good model performance (Minitab, 2017). For instance, the R^2 does not tell anything about data distortion or model competency.

Another common evaluation tool is to calculate the root of the mean of all errors made in the model, known as Root-Mean-Square-Error (RMSE):

$$\mathrm{RMSE} = \sqrt{\frac{\sum_{i=1}^{N}(\hat{x}_i - x_i)^2}{N}}, \tag{3.1}$$

where $\hat{x}_i$ represents each individual model prediction of the predicted component, x_i represents the corresponding measured value and N stands for the total number of data points. The higher the value, the more the data points are spread out from the regression line. The best fit, with a total correlation (R=1) between the observed and modelled values, signify zero as RMSE due to no distortion.

However, when using RMSE to evaluate model performance, individual errors can change their relative influence on the total error. In other words, taking the sum of squares of the errors the RMSE can unfortunately be increased by outliers and thus cause overestimations of the errors and, furthermore, underestimate the model performance (EOS, 2017). A comparable method is to use the absolute value of each difference and taking the mean of all the absolute errors, i.e. the mean absolute difference between the data points and the regression line, known as Mean-Absolute-Error (MAE):

$$\text{MAE} = \sqrt{\frac{\sum_{i=1}^{N} |\hat{x}_i - x_i|}{N}}. \tag{3.2}$$

By using this statistical method, none of the individual errors will overshadow another error and thus all the errors will be treated equally (EOS, 2017).

The RMSE as well as MAE is depending on the magnitude of the variables and give wrong information when comparing model performance in simulating different variables. Therefore, according to Taylor (2001), these can be made independent of their rating scales by normalizing them with the standard deviation (σ_{OBS}) of the observed value:

$$\text{sRMSE} = \frac{RMSE}{\sigma_{OBS}}, \tag{3.3}$$

or relative to the range of the observed values:

$$\text{nRMSE} = \frac{RMSE}{max_{OBS} - min_{OBS}}. \tag{3.4}$$

The same method is applied for normalization of MAE and is expressed as sMAE and nMAE.

4 Results and Discussion

4.1 Model evaluation

The model performance was evaluated by comparing measured turbulent fluxes against the modelled turbulent fluxes.

Figure 12 shows the median diurnal behaviour of both observed and modelled sensible and latent heat fluxes for each thermal season. Here the data coverage for the modelled fluxes are corrected to match the coverage of the observed fluxes for proper comparison (see Table 13 in Appendix C for data coverage). The first outstanding fact is that these figures indicate a relatively good model performance, especially for Q_E, where the modelled values follow closely the measured values. The diurnal difference between the maximum value of the modelled and observed Q_E in the different thermal seasons (e-h) are following: -15.5, -2.9, -3.4 and -5.9 W m^{-2}. This shows a slight model underestimation of Q_E, with largest underestimation occurring during the thermal winter. When looking closer at the difference respect to each hour, the model underestimates Q_E for all the hours in winter and autumn (largest differences are -18 and -7.6 W m^{-2}, respectively, for spring and summer: -6.6 and -3.4 W m^{-2}), whereas an overestimation occurs during noon in spring (max. 1.3 W m^{-2}) and summer. The diurnal behaviour of Q_E is best modelled in spring, which is also the case for Helsinki in Karsisto et al. (2016).

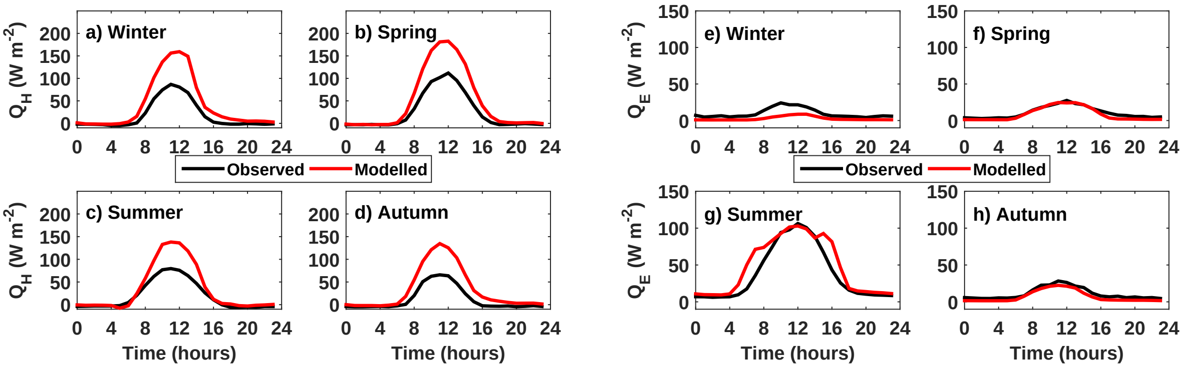

Figure 12. Median diurnal cycles shown in thermal seasons for observed (black) and modelled (red) sensible (a-d) and latent (e-h) heat fluxes. The data is for the 3-year study period. The fluxes are given in W m^{-2}.

For the sensible heat flux (Figure 12 a-d), the differences between the maximum values are notably greater, with similar calculations as above for Q_H: 72.7, 70.8, 58.5 and 68.9 W m^{-2}. The largest differences concerning all median hourly values are even higher: 80.8, 79.2, 60.3 and 68.9 W m^{-2}, respectively. The positive values indicate a model overestimation of Q_H. As well as for the latent heat flux, the largest positive differences are observed in winter and in spring, and the smallest in summer. Notably is that the smallest overestimation of Q_H and a slight underestimation of Q_H in the early morning hours occur in summer, simultaneously with the overestimation of Q_E in summer before (35.6 W m^{-2}) and after (38.3 W m^{-2}) noon (Figure 12 c and g). This could partly be explained that in SUEWS, the turbulent fluxes are competing of the same energy, thereby an underestimation in Q_E result an overestimation in Q_H. These findings confirm the statement made by Järvi et al. (2011), claiming that during daytime the latent heat flux is typically underestimated and the sensible heat flux is overestimated.

Additionally, the model performance can also be altered by outliers of -999 W m^{-2} included in the modelled values, which clearly differ from the observed absolute values of Q_E (-145 – 369 W m^{-2}) and Q_H (-87 – 346 W m^{-2}).

To have a deeper look at SUEWS performance, statistical tools were used (Table 9). The linear regression lines are shown in Figure 13 for both Q_H (top) and Q_E (bottom). The data evaluation is distinguished between all data and for different pollution categories (a and c) and thermal seasons (b and d). Notably is, when dividing the total hourly data based on pollution categories, less data are available due to the limits in obtaining AOD, resulting in only 16.4 % data available for the analysis. Even less data is available when adding the missing data for observed turbulent fluxes, leaving with a data coverage of 13.8 % and 14 % for Q_H and Q_E, respectively. For the division based on thermal seasons, on the other hand, only missing data concerning the observed fluxes influences the data coverage in this approach, resulting in a total data coverage of 84 % and 83,7 % for Q_H and Q_E, respectively. More precise information about data coverage in the different pollution categories can be found in Appendix C in Table 14 with the superscript of 2 and 3, and in Table 8 for the thermal seasons. To mention is that the diurnal behaviour of the fluxes shown in Figure 13 are calculated as median values per each hour in each thermal season, whereas the statistical measures are based on each residual separately and thereby takes all errors into account by either the mean of the absolute (MAE) or squared (RMSE) error.

Table 9. Model evaluation statistics relative to observations of sensible (Q_H) and latent (Q_E) heat fluxes for the three-year study period are given for the total data and divided into thermal seasons and pollution categories. Statistics used are: R^2 is the coefficient of determination, RMSE is the root mean square error (W m^{-2}, Equation 3.1), MAE is the mean absolute error (Equation 3.2) and the prefix *n* and *s* refers to the normalized errors (Equation 3.4 and 3.3). *N* stands for total number of data points. The AOD = 1 refers to AOD values higher than 1 and AOD = 4 to AOD values less or equal to 0.2, as marked in Figure 13.

Data division method		**R^2**	**RMSE** (W m^{-2})	**nRMSE**	**sRMSE**	**MAE** (W m^{-2})	**nMAE**	**sMAE**	***N*** (hours)
Total	Q_H	0.43	58.44	0.13	1.24	34.87	0.08	0.74	22079
	Q_E	0.33	55.60	0.11	1.14	29.60	0.06	0.61	22022
Thermal	Q_H	0.68	31.74	0.10	0.75	25.16	0.08	0.60	2341
Winter	Q_E	0.09	3.87	0.03	0.34	10.04	0.09	0.88	2353
Thermal	Q_H	0.64	45.38	0.12	0.82	31.61	0.08	0.57	3740
Spring	Q_E	0.17	22.31	0.09	1.17	13.57	0.06	0.71	3732
Thermal	Q_H	0.36	68.14	0.16	1.45	39.77	0.09	0.85	13238
Summer	Q_E	0.27	68.03	0.13	1.17	41.57	0.08	0.71	13161
Thermal	Q_H	0.54	33.74	0.13	0.92	24.06	0.09	0.66	2760
Autumn	Q_E	0.27	19.47	0.12	1.20	11.02	0.07	0.68	2776
AOD = 1	Q_H	0.42	59.64	0.20	1.26	58.53	0.19	1.24	828
	Q_E	0.23	58.37	0.15	1.11	38.22	0.10	0.73	833
AOD = 2	Q_H	0.40	68.11	0.22	1.27	65.32	0.21	1.22	879
	Q_E	0.37	63.99	0.16	1.06	40.88	0.10	0.67	879
AOD = 3	Q_H	0.38	75.05	0.19	1.24	69.99	0.18	1.15	1127
	Q_E	0.39	61.30	0.16	1.02	37.81	0.10	0.63	1137
AOD = 4	Q_H	0.34	77.23	0.21	1.22	60.91	0.17	0.96	800
	Q_E	0.41	68.68	0.21	1.09	42.03	0.13	0.67	841

Generally, the best simulated flux of these two turbulent fluxes is the latent heat flux, as already clear from the diurnal cycles. For the total data, the MAE for Q_E is 30 W m^{-2} compared to a larger distortion of the data points for Q_H (MAE = 35 W m^{-2}) and a lower nMAE of 0.06 compared to 0.08 for Q_H. The model underestimation of Q_E and overestimation of Q_H is also clearly visible in Figure 13.

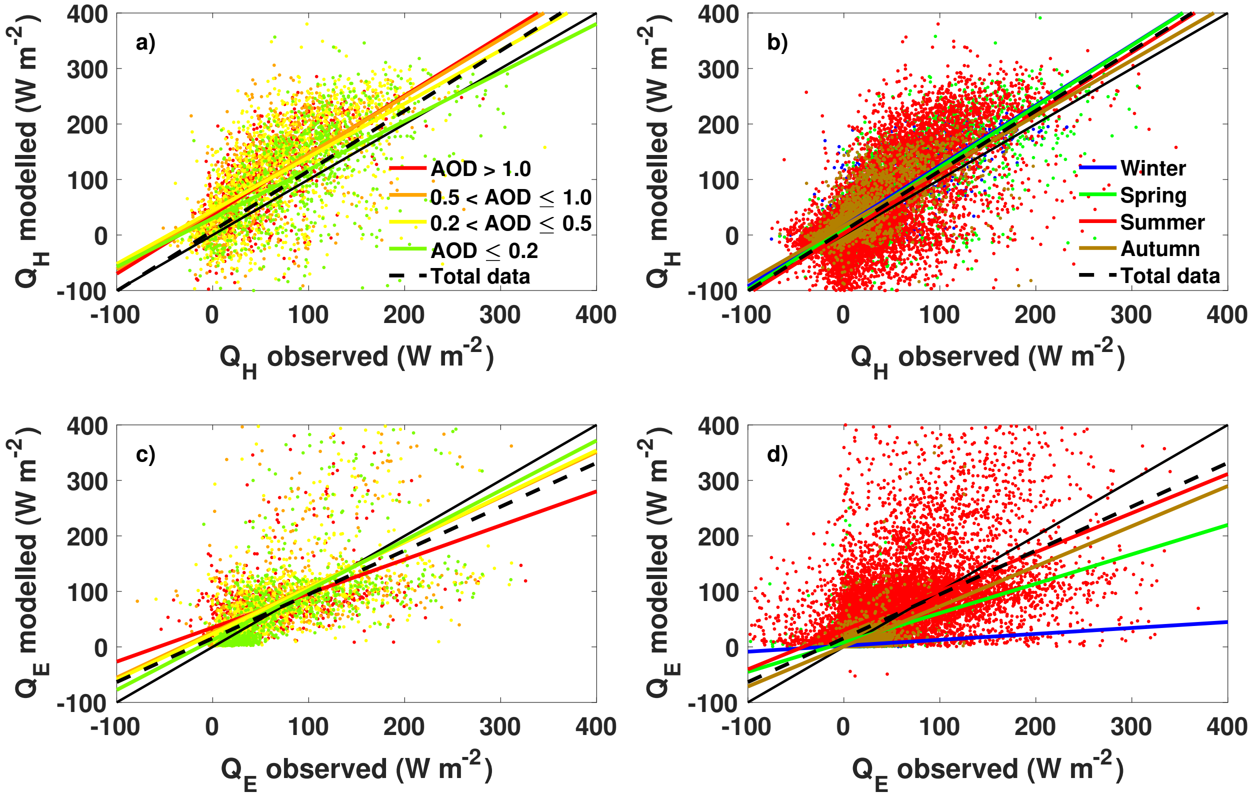

Figure 13. Scatter plots showing how the modelled turbulent fluxes (y-axis) correlate with the observed values (x-axis). The lines are linear fits for a line of first grade. Model performance is compared by dividing the available data into pollution categories (a and c) and by thermal seasons (b and d). The black solid line indicates the relation of 1:1, i.e. the perfect model performance. The black dashed line represents the fit for the total data available (see Appendix C and Section 3.4.1 for further information about data availability). Table 9 lists the model evaluation statistics concerning these plots.

When looking across the thermal seasons, the MAE for Q_E varies between 10−42 W m^{-2} (nMAE = 0.06−0.09), with best performance under thermal spring and poorer during winter and summer, as also stated above. The scatter is largest during the summer, with MAE values four times larger than for the thermal winter. The phase change related energy consumption during hot moist summers could be one of the reasons to the large uncertainty in modelling Q_E. However, the R^2 is higher for the summer and autumn, in comparison to the two other seasons, showing a better approximation, even though the spreading of the data is larger (higher MAE). According to Ward et al. (2016), SUEWS performance, evaluated in the UK, is generally better in summer than in winter.

For the sensible heat flux, the MAE varies between 24−40 W m^{-2} (nMAE = 0.08−0.09), which is a smaller range than for Q_E. In SUEWS, the Q_H is calculated as a residual from the other surface energy components in the Equation 2.3, leading to error accumulation in Q_H. Therefore, the model ability to simulate Q_H is influenced by possible errors occurring in the simulation of the other components. As it was for Q_E, the largest spread of the data points is during summer with the highest MAE, whereas the lowest nMAE is obtained during thermal spring and winter.

Additionally, model performance is analyzed by dividing the data into pollution categories (Figure 13 left, Table 9). A difference between the categories as well as between the turbulent fluxes is noticeable. Firstly, the scatter calculated for Q_E is almost half the nMAE values calculated for Q_H, varying from 0.10−0.13 (MAE = 38−42 W m^{-2}) for Q_E compared to Q_H (nMAE = 0.17−0.21 and MAE = 58−70 W m^{-2}), indicating a considerable better model performance in simulating Q_E than Q_H. An interesting observation is that the model performance for clear air situations is best for Q_H and worst for Q_E. For Q_E, an improvement in model performance is visible when the air becomes more polluted, whereas a similar trend for Q_H is not visible.

To have a better understanding of the impact of certain model parameters (Table 11 and 12 in Appendix A) and parametrizations, sensitivity analyses are made. The analysis includes increase in albedo for evergreen trees to maintain the same as for deciduous trees, use of standard SURFEX parameters defined for different surfaces (ECOCLIMAP, Masson et al., 2003), increasing building albedo, precluding the anthropogenic heat flux and changing the surface conductance parameters (not shown). During each sensitivity analysis, the other parameters or methods were held constant. In most cases, the impact was small or non-existent. Worth mentioning is that the use of standard parameters defined by surfex, a slight decrease in model performance was noticed, especially during thermal summer and spring. This verifies the importance of well-chosen and well-motivated parameter values, as proved by Grimmond et al. (2011). However, the aim of the study is not to evaluate model performance, therefore more sensitivity analyses were not made. In general, more sensitivity tests on a larger variety of parameter changes, such as for the surface conductance, need to be done to decrease the model errors and improve model performance.

The largest issue in SUEWS performance shown here is the observed model overestimation of Q_H, which compared to the underestimation of Q_E is larger in magnitude. There are a few thoughts concerning this issue. Equation 2.3 states that the components on the left-hand side, the available energy ($Q^* + Q_F$), need to be equally shared among the components on the right-hand side, including the Q_H. Firstly, one possible cause could be that the model overestimates the amount of the available energy in the system and this error of excess energy is then incorrectly accumulated in the Q_H component due to the model method of simulating Q_H as a residual term. The largest differences in the diurnal behaviours occur in winter, where the colder temperatures require more energy consumption, and consequently influencing Q_F. The Q_F is in general difficult to simulate and is modelled in SUEWS based on population density and heating and cooling degree days (HDD and CDD) (Järvi et al., 2011). The uncertainty concerning Q_F is commonly greater for urban centres compared to suburban areas due to more anthropogenic sources, thereby significantly impacting the amount of available energy and, furthermore, the estimation of the turbulent fluxes (Ward et al., 2016).

However, the sensitivity analysis of neglecting Q_F did not have any visible impacts on the model performance, so the reason could lie in the other SEB-components. A large contributor to the available energy is also the net all-wave radiation term (Q^*), that gains energy through incoming shortwave and longwave radiation and loses it through reflected shortwave radiation and emitted longwave radiation (Equaion 2.2). In this model run, $K\downarrow$ is given as meteorological forcing data, whereas the other three components are calculated inside the model, e.g. $L\downarrow$ is calculated based on observed air temperature and humidity data. According to Loridan et al. (2011), additional information about the cloud cover could improve model performance in calculating Q^*, because most errors are due to $L\downarrow$ calculations. Another interesting factor influencing the radiation, especially in Beijing, are aerosols in the air. When the air is more polluted, there is more potential for cloud formation, containing a large concentration of smaller cloud droplets and, furthermore, both decrease $K\downarrow$ and increase $L\downarrow$. Additionally, the Q_H was best simulated during clear air conditions, which could indicate that the aerosol direct or indirect effect as clouds could lead to more uncertainties in model simulations. Also during wet humid summers with monsoon conditions, with winds mostly blowing form the industrialized polluted areas in the south of Beijing, the model performance was lower than for other seasons. However, as measured $K\downarrow$ is used, the main aerosol effect is already included and thus, only $L\downarrow$ can cause errors in modelled Q^*.

However, if the error would be in modelling too low $L\downarrow$, it may result in model underestimation of Q^*, consequently not solving the problem of the modelled excess energy. On the other hand, the error could also be in calculating the upward radiative fluxes, which are both dependent on the plan are fractions together with either surface albedo (in $K\uparrow$) or surface emissivity (in $L\uparrow$). Sensitivity test show, however, that the surface albedo is an unlikely reason for the overestimation of Q^*. One other explanation could be the plan area fractions, which alter the model performance the most (Grimmond et al., 2011). The fractions were here determined based on available satellite images, which of course enable errors in Q^* and maybe also in simulating Q_E. Unfortunately, with no available observations of Q^*, model evaluation of Q^* was not possible and therefore it is difficult to determine whether Q^* is in eventually underestimated or overestimated.

Secondly, apart from calculations of Q^* and Q_F, the problem could also be in the calculation of ΔQ_S (right hand side of Equation 2.3). Especially during wintertime, when Q^* has a smaller impact by less incoming solar radiation, the problems related to Q_H simulations could be due to Q_F and/or ΔQ_S. An underestimation of ΔQ_S could be due to a model overestimation of the nocturnal heat release, causing the net storage heat to be too small (Song et al., 2013; Ward et al., 2016). SUEWS calculates ΔQ_S using defined OHM-coefficients, containing information about surface materials and surface thermal parameters. The choice of parameters in the OHM coefficients could improve Q_H considerably, taking the seasonality into account (Ward et al., 2016). Added to this, the model uses Q^* for ΔQ_S simulation, which also highlights the importance in simulating Q^* correctly.

The third possible explanation for the shown model performance could be in the latent heat flux.

The heat and water exchange between the surface and the atmosphere, defined by the surface conductance and soil moisture deficit parameters, have a large impact on the calculation of Q_E (Järvi et al., 2011). Periodicity of precipitation could also impact the simulation of Q_E, determining when there will enough available water for Q_E. Moreover, during the dry period, the water sources to the system originate from either irrigation or the ground, which both induce challenges for the model. The assumption of zero irrigation during winter months could therefore explain the underestimation of Q_E during winter, whereas in autumn the hot and dry climate conditions in Beijing result in intense irrigation and thus give rise to higher observed Q_E than simulated. Additionally, seasonal changes in LAI, especially in spring or early summer with rapid leaf growth, affects Q_E, which, in comparison to fixed profiles used in many models, varies dynamically in SUEWS depending on the air temperature (Karsisto et al., 2016). However, here the Q_E is well modelled.

Furthermore, energy removal through advection is not separately modelled as energy output, which could explain the energy excess input in the system and the overestimation of Q_H due to Q_E being calculated as a residual.

Notably is also that the turbulent fluxes measured by EC technique used in the model evaluation also have its disadvantages. The energy flux components vary spatially depending on the surface characteristics and the heterogeneous surface cover in urban areas, with estimated source areas changing by measurement height, wind speed and direction, stability and the roughness of the surface (Schmid et al., 1991). EC measurements are usually done at $2-3$ times the mean building height in order to catch all the heterogeneous areas that act as source areas for the fluxes (Song et al., 2013). The surface cover fractions determined for this study are therefore only estimations for the influenced area of approximately 1 km radius circle around the tower. Additionally, the observed precipitation data were taken 10 km apart from the tower, which due to its occasionally locally appearance, does not represent the true climate conditions valid exactly at the tower and could thereby affect the model performance.

It is obvious that most model uncertainties are related to processes that are difficult to measure, such as heat storage or anthropogenic heat fluxes, which together with the choice of input parameter values, meteorological forcing data and calculation methods used in the models have huge impact on model performance. Despite the systematic errors and lack of total resemblance between the modelled and measured turbulent fluxes, the model performance is good enough for the purpose of this study. Therefore, for the analysis made in the following chapters, the modelled SEB components are used.

4.2 Modelled components of the urban surface energy balance

Monthly averaged modelled components in the urban surface energy balance equation (2.3) for Beijing are shown in Figure 14. The different colours indicate the different components as defined in the legend and the mean values of the fluxes are calculated for each month and study year separately. Here positive mean values refer to energy added to the system (input) and negative mean values refer to energy removal from the system (output). The energy balance closure is achieved on each year. Following diurnal and statistical analysis, the general behaviour of the turbulent heat fluxes are well simulated by the model, where larger energy supply is found in summer due increased solar energy, whereas less available energy is simulated for the winter months.

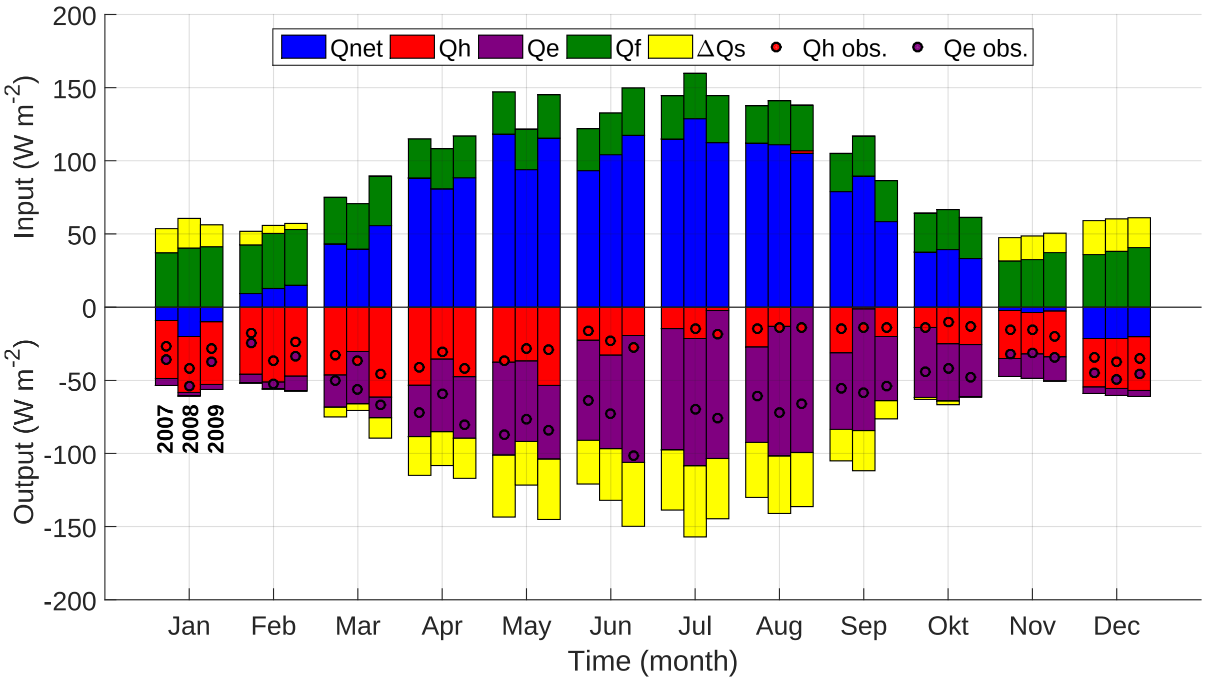

Figure 14. Monthly average surface energy balance components for Beijing. Each month has three bars, one bar for each year of the observation period 2007−2009. The different fluxes are marked with different colours and separated into input and output parts. Additionally, the coloured circles show the monthly averages of the observed Q_E and Q_H components. Note that there are no circles for July 2007 due to missing observations for this month. Note also the different data coverages concerning the modelled and measured turbulent fluxes.

Additionally, there is a clear monthly variation in the relative importance of the different fluxes. Q^* receives negative values in winter (-21 W m^{-2} in December 20007), which is to be expected due to less solar energy, resulting in small $K\downarrow$ and $L\downarrow$ (Järvi et al., 2014) and larger out-radiation (Bergeron and Strachan, 2012). Another possible explanation for the negative values could be smaller $L\downarrow$ due to drier conditions, prohibiting cloud formation and further decrease $L\downarrow$. Worth mentioning is that these values are mean values taking all hours in the day into consideration, without distinguishing between night and day.

Within the year, the absolute amount of Q^* increases followed by increased solar radiation, reaching its peak in July (128 W m^{-2} in July 2008). The increased humidity and water vapour concentrations in the air due to the summer monsoon conditions could also be possible reasons to the increase in Q^*. Obviously, due to $K\downarrow$, Q^* stands for the main share of the available energy between March and October, coinciding with the wet period occurring from May to October as defined by Liu et al. (2012).

The second important component participating in the amount of available energy is the anthropogenic heat flux (Q_F). On the whole, the total available energy is high in urban sites due to the added energy input by Q_F (Bergeron and Strachan, 2012). The monthly variation of Q_F is considerably smaller compared to Q^*, ranging from 26 W m^{-2} to 41 W m^{-2}, showing that this flux is an important heat input throughout the year. During colder temperatures in winter, when the need of heating is large, the absolute values of modelled Q_F are slightly higher than in other seasons. From November to February, the Q_F acts as the most important energy input (Figure 14). Similar results were obtained by Offerle et al. (2005), where the Q_F was calculated as a residual term and resulted in 60 % of the available energy from October to March in Poland.

The third component that partly contribute to the energy input to the system is the net storage heat flux (ΔQ_S), ranging from -23 W m^{-2} in December 2007 to 49 W m^{-2} in July 2008. This is a logically following the trend in Q^* due to energy storage to the ground. ΔQ_S is negative when heat is released from the ground and city structures, contributing to an energy input to the system in winter, whereas positive values indicate that heat is stored, thus contributing to energy output from the system in summer. The ΔQ_S contributes less than a half of the energy supply during winter months, when the energy supply from Q_F is of most importance. It is shown, that this component in general is an important term in the SEB (Offerle et al., 2005; Grimmond and Oke, 1999b). This can also be seen in Table 10, where the share of ΔQ_S compared to the available energy ($Q^* + Q_F$) increases towards the summer, accounting for almost 30 % of the available energy. This is also confirmed by Bergeron and Strachan (2012), where its fraction of the available energy in urban areas in Montreal increases towards the summer, reaching almost 45 % when only taking the daytime monthly means into account. Likewise, Grimmond and Oke (1999b) calculated a contribution of 17−58 % of the available energy during daytime in North America.

The two last components of the SEB are the turbulent sensible heat (Q_H) and latent heat (Q_E) fluxes. There is a visible anti-correlation between the appearance of these two: the Q_H reaches its monthly maximum in March (61 W m^{-2} in 2009) almost simultaneously when Q_E reaches its minimum (3 W m^{-2} in January 2008). The Q_H decreases then towards summer, obtaining its minimum values in late summer (-2 W m^{-2} in August 2009), whereas oppositely the Q_E increases, obtaining its maximum monthly average value of 101 W m^{-2} in July 2009. In other words, at the start of the year, most of the available energy is consumed by the Q_H, accounting for in average 59 % of the available energy in March, accompanied with

31 % for Q_E and only 11 % for ΔQ_S (Table 10). These relative portions changes suddenly, resulting in a transition period between the turbulent fluxes in spring. In June, the Q_E accounts for over the half of the available energy, followed by 27 % for ΔQ_S and 19 % for Q_H. Q_E maintains its position as main energy consumer throughout the summer and early autumn, experiencing the next transition in November. Same trend for Q_E of being the dominant term during summer and Q_H in spring is also proven by Liu et al. (e.g. 2012). The impact of LAI, being at its maximum in summer and decreasing during dry periods, could be one reason for the seasonal behaviour of Q_E. The trend during the wet period in summer further show how almost no energy is remained for Q_H after being used for evaporation (highest portion consumed by Q_E) and ΔQ_S. The slightly negative values in the simulation of Q_H could therefore be due to possible model errors.

Table 10. The portion of the sensible heat flux (Q_H), latent heat flux (Q_E) and storage heat flux (ΔQ_S) with respect to the available energy ($A = Q^* + Q_F$) shown per month and for each year separately and as a 3-year mean. The values are related to the mean values calculated for each component in the SEB equation (2.3), illustrated in Figure 14.

	Jan	Feb	Mar	Apr	May	Jun	Jul	Aug	Sep	Oct	Nov	Dec
	2007											
Q_H / A	1.42	1.08	0.62	0.46	0.26	0.19	0.10	0.20	0.30	0.21	1.12	2.28
Q_E / A	0.17	0.14	0.29	0.31	0.43	0.56	0.57	0.47	0.50	0.75	0.42	0.31
ΔQ_S / A	-0.59	-0.22	0.09	0.23	0.29	0.25	0.28	0.27	0.20	0.02	-0.54	-1.59
	2008											
Q_H / A	1.88	1.01	0.43	0.33	0.30	0.25	0.14	0.09	0.01	0.38	0.98	2.03
Q_E / A	0.12	0.09	0.51	0.46	0.45	0.48	0.55	0.63	0.71	0.59	0.58	0.28
ΔQ_S / A	-1.00	-0.11	0.06	0.21	0.24	0.27	0.30	0.28	0.23	0.04	-0.56	-1.31
	2009											
Q_H / A	1.37	0.89	0.69	0.41	0.37	0.13	0.02	-0.01	0.23	0.42	0.91	1.80
Q_E / A	0.11	0.19	0.16	0.36	0.35	0.58	0.70	0.73	0.51	0.58	0.48	0.20
ΔQ_S / A	-0.48	-0.08	0.15	0.23	0.28	0.29	0.28	0.27	0.14	-0.00	-0.39	-0.99
	3-year average											
Q_H / A	1.52	0.99	0.59	0.40	0.31	0.19	0.09	0.09	0.17	0.34	1.00	2.01
Q_E / A	0.13	0.14	0.31	0.37	0.41	0.54	0.60	0.61	0.58	0.64	0.49	0.26
ΔQ_S / A	-0.65	-0.13	0.11	0.23	0.27	0.27	0.29	0.27	0.20	0.02	-0.49	-1.26

4.3 Connection between aerosols and the surface energy components

In this section, general behaviour of AOD is discussed and the impact of aerosols on the modelled SEB components is analyzed, with emphasize on the sensible and latent heat fluxes calculated for Beijing. As listed in Table 7, on an hourly basis, most data fall into the third pollution group (light polluted air), accounting for 32 % of the total data, whereas the fairly clean air category accounts for least data, 22 % of the total. The extreme polluted air (category 1) is achieved for 24 % of the time of the available AOD-data.

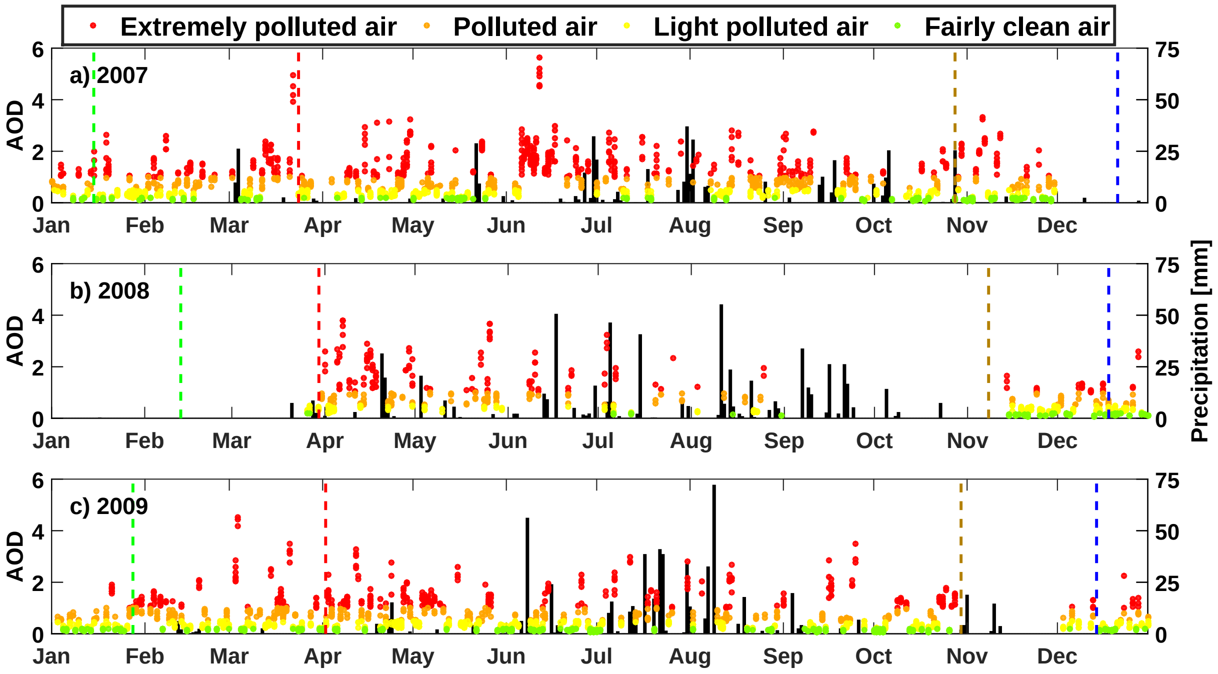

Figure 15. Measured AOD (left axis) divided into four groups of pollution categories together with observed daily precipitation (right axis). The AOD values on the same vertical line show multiple AOD measurements taken for one day. The vertical stacked lines indicate the start of each thermal season for each observation year.

Figure 15 shows the annual behaviour of AOD points together with observed daily precipitation for each year separately. Additionally, vertical dashed lines show the start of each thermal season on different years (see Section 3.5). The figure clearly shows the periods when AOD data are available, as well as missing data. There is a gap in the data from end 2009 until the start of the thermal summer in 2008, same as for end of the summer 2008 and in autumn 2009. Interesting is the low or missing AOD-data for the end of the thermal summer in 2008, which coincide with the time straight following the Summer Olympic games in Beijing in August 2008. The planned improvements in the air quality due to the games (Streets et al., 2007) could partly explain lower measured AOD in 2008 compared to the same time in 2007 or 2009. Although restrictions were made, high values measured again in 2009 show how the air quality can quickly worsen back again, and the impact of the restrictions were not long-lasting. However, in this study, this matter was not explored in more detail.

The daily median AOD-values calculated based on the available hourly AOD-data are illustrated in the upper timeserie in Figure 8, where the highest daily value of 4.9 is measured on 12^{th} of June 2007 and the lowest value of 0.07 on 18^{th} of October 2007. On an hourly basis, maximum AOD value measured is 5.6, coinciding with the same day as highest daily value, whereas the lowest value of 0.05 is measured on 29^{th} of November 2007. The anthropogenic activity is clearly visible in AOD observed in Beijing due to high AOD measured throughout the year (Figure 15).

However, the relative number of elements in the pollutant category 1 differ between the different thermal seasons, showing a clear seasonal variation in the AOD-data. As listed in Table 14 (superscript 1) shown in Appendix C, only 8 % of the total AOD-data for the thermal winter belong to the category 1. This portion is, however, rising, where extreme polluted conditions are accounted for 24 % in spring, reaching its peak in summer with 27 % and then decreasing down to 16 % in autumn. Comparably, same portions for the clear air conditions, pollution category number 4, are 39 % in winter, decreasing to 19 % in spring, until 18 % in summer and eventually increasing to 38 % in autumn. This seasonal difference signifies small aerosol values in winter and high values in the summer. Sundström et al. (2012) is discussing this phenomenon. The dry period is signified by prevailing northerly winds, improving the air quality in winter. During the wet period, the prevailing winds are from the south and southeast (Liu et al., 2012), transporting pollutants from the surrounding to more industrialized provinces, such as Hebei and Tianjin (Streets et al., 2007). The poor air quality is further influenced by the mountain range in the north, enabling pollution accumulation and thereby worsen the air quality even further. On the other hand, the aerosols, as explained, act as condensation nuclei for cloud formation and thereby further strengthen the possibility of precipitation events. Rain cleans the air and decreases the residence time of aerosol in the air (Sundström et al., 2012). There is a slight correlation of lower AOD- values after rain events compared to the values before rain (not shown), which can also partly be seen in Figure 15. However, AOD- data as well as the precipitation data are not observed at the meteorological tower, which impacts the correlation due to AOD calculation technique as column average and lack of proper precipitation observations at the study site. On the other hand, moisture, increased air temperature together with stagnant air can lead to the formation of smog, which tends to increase the AOD values (Sundström et al., 2012; Streets et al., 2007). The peaks in the AOD- data during summer could be signs from these smog events. In autumn, relatively high values are still measured, showing that Beijing is still affected by more polluted air transported from the south. Additionally, high AOD-values are also measured during spring, at the time when the northerly winds weaken, being more influenced by the monsoon winds from the south. The weaker winds enable the air to mix, which together with higher air temperatures and moisture further increases the residence time of aerosols in the air (Sundström et al., 2012). Added to this, even dust-outbreaks from the Gobi-desert could influence the air quality during spring. On the other hand, northern part of China has less-polluted areas, and the northerly winds transport cleaner air over north-eastern part of China, which in some cases can be seen as decreasing AOD values.

As a summary, the air conditions in Beijing is hazardous and it is obvious that they will have an impact on the human health as well as influencing climate conditions.

The impact aerosols have on the SEB is investigated next by looking at the median values calculated for each thermal season (Figure 16). The data are further divided into the different pollution categories.

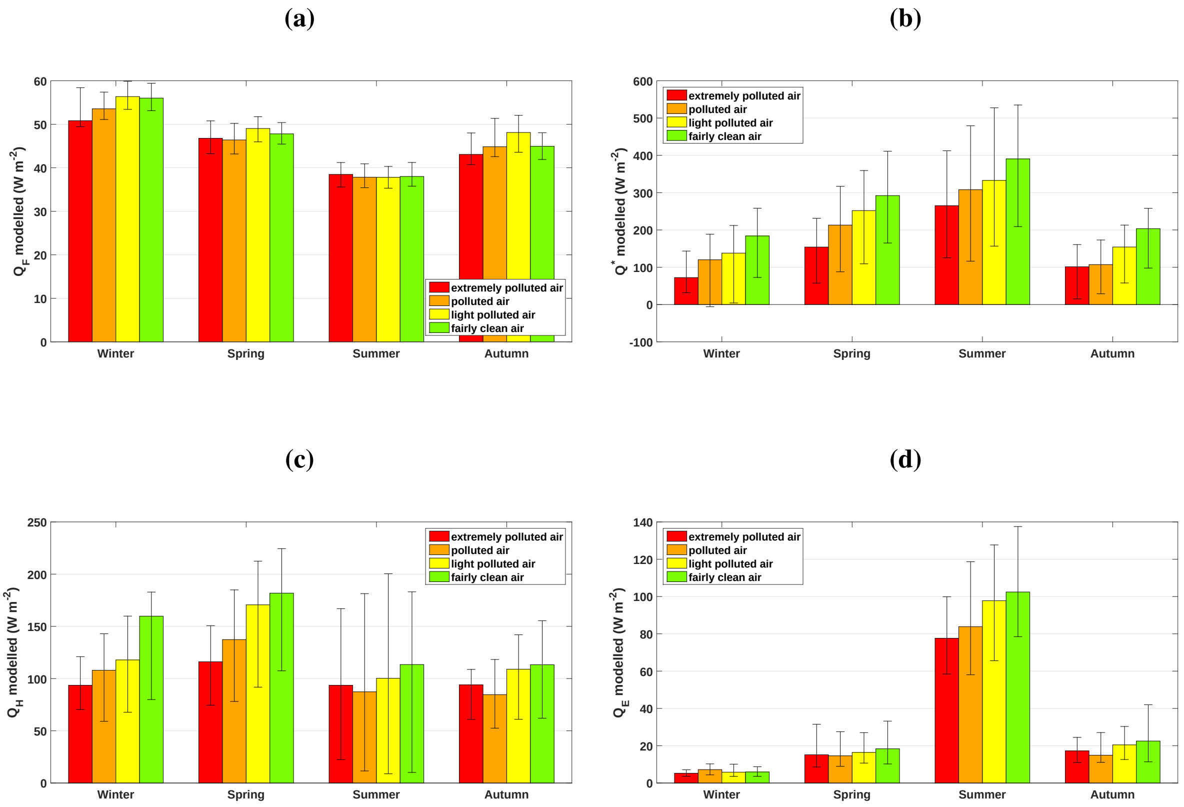

Figure 16. Error bar plots showing the median values of modelled **(a)** anthropogenic heat flux (Q_F), **(b)** net all-wave radiation (Q^*), **(c)** sensible heat flux (Q_H) and **(d)** latent heat flux (Q_E) for each pollution category, separated into thermal seasons. The error bars indicate the 25^{th} and 75^{th} quartiles. The storage heat flux (ΔQ_S) is now left out of the analysis. Data coverage in this analysis is based on the available AOD- data according to Table 14 as superscript 1, found in Appendix C.

As stated in the last chapter, the Q_F is nearly constant throughout the year, with slightly higher values in the colder seasons. Due to the low variability in the absolute values of Q_F, the range between 25$-$75 % of the mean values is rather small. For Q_F there is no distinct difference between the pollution categories in the different thermal seasons (Figure 16a). In summer, the difference between clear conditions and very polluted conditions is -0.5 W m^{-2}, whereas in other seasons, the difference is slightly positive, with 5.2 W

m^{-2} calculated for the winter season.

In Q^*, on the other hand, an obvious difference in different pollutant categories is visible (Figure 16b). The corresponding differences between clean and polluted air conditions for each thermal season related to Q^* are: 112, 138, 126 and 102 W m^{-2}, showing the largest difference during summer and spring, and less aerosol influence during times with less incoming solar radiation (in winter and autumn). The clear impact the air pollutants have on Q^* was to be expected due to their radiative properties. The greatest difference is visible during the time with more incoming solar radiation ($K \downarrow$). The diurnal behaviour of $K \downarrow$ shown in Figure 4 further confirms the result of the aerosol radiative effects in decreasing $K \downarrow$. In winter, however, the radiative effects of aerosols on the longwave radiation could be of more importance (Garrett et al., 2002), and thereby influencing Q^* by showing less difference for colder seasons. However, for all thermal seasons, the median value calculated for Q^* is increasing with improved air quality.

The two bottom-one figures show the effect air pollutants have on the sensible heat flux (Q_H) and latent heat flux (Q_E) (Figure 16c and 16d). Notably, there are big uncertainties regarding the Q_H, especially in summer, whereas for the Q_E the range is clearly smaller. This could be due to the method in the model to calculate Q_H as a residual term, attenuating the model errors when calculating other fluxes in summer. The turbulent fluxes are largely dependent on the climate in Beijing, where the relative share of how the energy is divided by the turbulent fluxes is affected by the dry and wet periods, contributing to available water and further impacting the evaporation. Apart from the climate, there is a distinct difference between median values of the turbulent fluxes when analyzing the data considering the air quality. The clear impact aerosols have on the Q^* is obviously reflected to the turbulent fluxes, due to their dependency on the available energy. For winter and spring, when Q_H is the most important turbulent flux, it is continuously increasing per improved air quality. In summer and autumn, a slight decrease between the two polluted categories is noticeable, but, is in general increasing with improved air quality (Figure 16c). The calculated differences between the two extreme pollution categories (category one and four) in the different thermal seasons for Q_H are: 66, 66, 20 and 19 W m^{-2}, which further shows that the smallest difference occur in summer. Same dependence was investigating using the observed data of Q_H (not shown), where a trend of a continuous increase of Q_H was visible for all the thermal seasons, accounting for comparable differences of: 62, 91, 32 and 61 W m^{-2}.

Comparable findings apply even for Q_E. In summer, when most of the available energy is consumed by Q_E, the aerosol impact on Q_E is likewise most visible (see Figure 16d). The corresponding differences between the clear and polluted air conditions for the modelled Q_E in the different thermal seasons are following: 0.7, 3, 25 and 5 W m^{-2}. As it was for Q_H, a slight deviation from the continuous increase in the flux by improved air quality is notable between category one and two for all other thermal seasons except for summer, where the increase is continuous for each improved pollution category. In winter, when Q_E is small due to the influence of LAI and less incoming solar radiation and moisture, the aerosol impact remains likewise small. Similar as for Q_H, same analysis was made using the observed Q_E data, where an increase of Q_E by improved air quality was to be seen (not shown). The corresponding differences for the observed Q_E data are: 12, 15, 46 and 19 W m^{-2}. As for Q_H, the dependence of air quality on the turbulent energy fluxes is more visible when analyzing the observed data due to bigger absolute differences, but the behaviour of the fluxes is still reproduced by the model. The aerosol impact is therefore evident in the analysis made using the modelled components.

5 Conclusions

An urban surface energy and water balance model (SUEWS) is run for a neighbourhood located in the north-western part of Beijing, China, to study the components of the urban surface energy balance for the study period of 3 years (2007−2009). Additionally, using measured aerosol data for describing the prevailing pollution conditions during the study period, the effect of air quality on the different modelled surface energy balance components is examined. Observations from EC measurements of the turbulent sensible and heat fluxes measured at the Beijing meteorological tower are further used to evaluate model performance. The model evaluation shows a general model underestimation of Q_E and a more distinct model overestimation of Q_H. Uncertainties in modelling occur due to used parametrizations, observation representability and chosen site specific parameters, highlighting the importance in understanding what measurements are used and what input parameters are required by the model. Despite the errors appeared in the model evaluation, the model is still able to simulate the behaviour of the evaluated turbulent fluxes well.

The modelled components are shown to have a clear monthly as well as seasonal and periodic variability. The anthropogenic heat flux was relatively constant throughout the year, whereas the net all-wave radiation changed followed mostly by the available solar radiation. The available energy defined the energy disposable for the turbulent fluxes, where the dry and wet periods further defined the relative share of each turbulent flux. Thereby, during cold and dry periods, the sensible heat flux was shown to be the dominating flux, with maximum contribution of 59 % of the available energy in early spring. However, due to an increase in humidity and precipitation, allowing evaporation to occur, together with increased values of LAI, the share between the turbulent fluxes is quickly shifted. In summer, the sensible heat flux accounted for only 20 % of the available energy, whereas the latent heat flux clearly dominated and accounted for over half of the available energy. The storage heat flux is additionally shown to be an important term in the SEB, accounting for, on average, one fourth of the available energy, acting as a source (sink) for the energy in the system during winter (summer).

The focus of this study was, however, to examine how the behaviour of the SEB-components is modified by the atmospheric aerosol particles. The measured AOD data showed seasonal differences in air quality conditions in Beijing. Better air quality conditions were shown to occur in winter compared to higher AOD-values measured during the thermal summer, which confirms how the air quality in Beijing is affected by the terrain, climate, such as wind and precipitation, and surrounding districts. Least of the days belonged to the pollutant category of fairly clean air conditions, which further verifies the severe air conditions found in Beijing.

Attenuation of the incoming solar radiation due to the radiative properties of the aerosols, thereby affecting the net-radiative flux, is a well-known phenomenon, which is also visible in the results presented in this study. For all thermal seasons, the net radiative flux was shown to increase by improved air quality, resulting in the largest difference of 138 W m^{-2} calculated for spring. The anthropogenic flux did not show any clear aerosol impact. Similar impact of haze, as for the net-radiative flux, is visible for the turbulent energy fluxes. An interesting finding is that the largest impact aerosols have on the turbulent fluxes occurs exactly during the thermal season, when the turbulent flux in question accounts for the most part of the available energy. Results show that the largest aerosol impact on the sensible heat flux occurs during thermal spring, resulting in a difference of 66 W m^{-2} between clean and very polluted conditions. Likewise, in summer, when the latent heat flux is the largest contributor for consuming the available energy, the influence of aerosols is most visible, resulting in 25 W m^{-2} higher values with improved air quality. The differences calculated for observed turbulent fluxes show even larger differences and clearer aerosol impact.

As a summary, aerosols are shown to be able to modify not only the radiative fluxes in the surface energy balance, but also to influence the turbulent heat fluxes, causing these fluxes to decrease by poorer air quality. This could further alter the urban climate, seen as possibly higher surface temperatures, through decreased sensible heat flux, and increased runoff and higher risk of flooding, through less energy available for evaporation of the precipitated water due to decreased latent heat flux. However, further investigations are needed to fully determine the impact of aerosols on the sensible and heat fluxes, as well as to evaluate their further impact on other components in the urban climate. The results presented in this study highlight the importance of aerosols and give an insight in their ability to modify the components related to the urban surface energy balance. Therefore, the findings of this study could be helpful in urban planning and issues related to water management and air pollution restrictions.

Bibliography

AQICN (2017). Beijing air pollution: Real-time air quality index (aqi). `http://aqicn.org/city/beijing/`. [Online; data accessed 17-8-2017].

Atwater, M. A. (1971). The radiation budget for polluted layers of the urban environment. *Journal of Applied Meteorology*, 10(2):205–214.

Baldocchi, D. D. (2003). Assessing the eddy covariance technique for evaluating carbon dioxide exchange rates of ecosystems: past, present and future. *Global change biology*, 9(4):479–492.

Bergeron, O. and Strachan, I. B. (2012). Wintertime radiation and energy budget along an urbanization gradient in montreal, canada. *International Journal of Climatology*, 32(1):137–152.

Brunekreef, B. and Holgate, S. T. (2002). Air pollution and health. *The lancet*, 360(9341):1233–1242.

Campbell Scientific (2017). 3-d sonic anemometer. `https://www.campbellsci.com/csat3a`. [Online; data accessed 1-5-2017].

Chang, C.-P. (2004). *East Asian Monsoon*, volume 2. World Scientific.

City Population (2014). China: Administrative division of beijing, district and township. china national bureau of statistics. `http://www.citypopulation.de/php/china-township-beijing-admin.php`. [Online; data accessed 1-6-2015].

CORDIS (2016). Urban report summary. `http://cordis.europa.eu/result/rcn/185709_fr.html`. [Online; data accessed 1-9-2017].

Demuzere, M., Harshan, S., Järvi, L., Roth, M., Grimmond, C., Masson, V., Oleson, K., Velasco, E., and Wouters, H. (2017). Impact of urban canopy models and external parameters on the modelled urban energy balance in a tropical city. *Quarterly Journal of the Royal Meteorological Society*, 143(704):1581–1596.

DieselNet (2002). Diesel exhaust particle size. `https://www.dieselnet.com/tech/dpm_size.php`. [Online; data accessed 7-9-2017].

Dockery, D. W. and Pope, C. (2014). Lost life expectancy due to air pollution in china. *Risk Dialogue Magazine*, 17:5–11.

EOS (2017). Climate and other models may be more accurate than reported. `https://eos.org/opinions/climate-and-other-models-may-be-more-accurate-than-reported`. [Online; data accessed 21-9-2017].

Esri Inc (2015). About arcgis. `http://www.esri.com/arcgis/about-arcgis`. [Online; data accessed 31-8-2015].

Estournel, C., Vehil, R., Guedalia, D., Fontan, J., and Druilhet, A. (1983). Observations and modeling of downward radiative fluxes (solar and infrared) in urban/rural areas. *Journal of Climate and Applied Meteorology*, 22(1):134–142.

FMI (2017). Termiset vuodenajat. `http://ilmatieteenlaitos.fi/termiset-vuodenajat`. [Online; data accessed 14-6-2017].

Gao, J., Wang, T., Zhou, X., Wu, W., and Wang, W. (2009). Measurement of aerosol number size distributions in the yangtze river delta in china: Formation and growth of particles under polluted conditions. *Atmospheric Environment*, 43(4):829–836.

Garrett, T. J., Radke, L. F., and Hobbs, P. V. (2002). Aerosol effects on cloud emissivity and surface longwave heating in the arctic. *Journal of the Atmospheric Sciences*, 59(3):769–778.

Grimmond, C., Blackett, M., Best, M., Baik, J.-J., Belcher, S., Beringer, J., Bohnenstengel, S., Calmet, I., Chen, F., Coutts, A., et al. (2011). Initial results from phase 2 of the international urban energy balance model comparison. *International journal of climatology*, 31(2):244–272.

Grimmond, C., Blackett, M., Best, M., Barlow, J., Baik, J., Belcher, S., Bohnenstengel, S., Calmet, I., Chen, F., Dandou, A., et al. (2010). The international urban energy balance models comparison project: first results from phase 1. *Journal of applied meteorology and climatology*, 49(6):1268–1292.

Grimmond, C., Cleugh, H., and Oke, T. (1991). An objective urban heat storage model and its comparison with other schemes. *Atmospheric Environment. Part B. Urban Atmosphere*, 25(3):311–326.

Grimmond, C., Oke, T., and Steyn, D. (1986). Urban water balance: 1. a model for daily totals. *Water Resources Research*, 22(10):1397–1403.

Grimmond, C. and Oke, T. R. (1999a). Aerodynamic properties of urban areas derived from analysis of surface form. *Journal of applied meteorology*, 38(9):1262–1292.

Grimmond, C. and Oke, T. R. (1999b). Heat storage in urban areas: Local-scale observations and evaluation of a simple model. *Journal of applied meteorology*, 38(7):922–940.

Grimmond, C. and Oke, T. R. (2002). Turbulent heat fluxes in urban areas: observations and a local-scale urban meteorological parameterization scheme (lumps). *Journal of Applied Meteorology*, 41(7):792–810.

Grimmond, C. S. B. and Oke, T. R. (1991). An evapotranspiration-interception model for urban areas. *Water Resources Research*, 27(7):1739–1755.

Han, L., Zhou, W., Li, W., and Li, L. (2014). Impact of urbanization level on urban air quality: a case of fine particles (pm 2.5) in chinese cities. *Environmental Pollution*, 194:163–170.

Haywood, J. and Boucher, O. (2000). Estimates of the direct and indirect radiative forcing due to tropospheric aerosols: A review. *Reviews of geophysics*, 38(4):513–543.

Holben, B. N., Eck, T., Slutsker, I., Tanre, D., Buis, J., Setzer, A., Vermote, E., Reagan, J., Kaufman, Y., Nakajima, T., et al. (1998). Aeronet—a federated instrument network and data archive for aerosol characterization. *Remote sensing of environment*, 66(1):1–16.

Järvi, L., Grimmond, C., and Christen, A. (2011). The surface urban energy and water balance scheme (suews): Evaluation in los angeles and vancouver. *Journal of hydrology*, 411(3):219–237.

Järvi, L., Grimmond, C. S. B., Taka, M., Nordbo, A., Setälä, H., and Strachan, I. B. (2014). Development of the surface urban energy and water balance scheme (suews) for cold climate cities. *Geoscientific Model Development*, 7:1691–1711.

Karsisto, P., Fortelius, C., Demuzere, M., Grimmond, C. S. B., Oleson, K., Kouznetsov, R., Masson, V., and Järvi, L. (2016). Seasonal surface urban energy balance and wintertime stability simulated using three land-surface models in the high-latitude city helsinki. *Quarterly Journal of the Royal Meteorological Society*, 142(694):401–417.

Kokkonen, T., Grimmond, C., Räty, O., Ward, H., Christen, A., Oke, T., Kotthaus, S., and Järvi, L. (2017). Sensitivity of surface urban energy and water balance scheme (suews) to downscaling of reanalysis forcing data. *Urban Climate, https://doi.org/10.1016/j.uclim.2017.05.001*.

Kulmala, M., Vehkamäki, H., Petäjä, T., Dal Maso, M., Lauri, A., Kerminen, V.-M., Birmili, W., and McMurry, P. H. (2004). Formation and growth rates of ultrafine atmospheric particles: a review of observations. *Journal of Aerosol Science*, 35(2):143–176.

Lamb, D. and Verlinde, J. (2011). *Physics and chemistry of clouds*. Cambridge University Press.

Lawrence, D. M., Oleson, K. W., Flanner, M. G., Thornton, P. E., Swenson, S. C., Lawrence, P. J., Zeng, X., Yang, Z.-L., Levis, S., Sakaguchi, K., et al. (2011). Parameterization improvements and functional and structural advances in version 4 of the community land model. *Journal of Advances in Modeling Earth Systems*, 3(1).

Licor Inc (2017). Open path gas analyzer. `https://www.licor.com/env/products/gas_analysis/LI-7500RS/`. [Online; data accessed 1-5-2017].

Lindberg, F., Grimmond, C. S. B., Yogeswaran, N., Kotthaus, S., and Allen, L. (2013). Impact of city changes and weather on anthropogenic heat flux in europe 1995–2015. *Urban Climate*, 4:1–15.

Liu, H., Feng, J., Järvi, L., and Vesala, T. (2012). Four-year (2006–2009) eddy covariance measurements of co 2 flux over an urban area in beijing. *Atmospheric Chemistry and Physics*, 12(17):7881–7892.

Loridan, T., Grimmond, C., Offerle, B. D., Young, D. T., Smith, T. E., Järvi, L., and Lindberg, F. (2011). Local-scale urban meteorological parameterization scheme (lumps): longwave radiation parameterization and seasonality-related developments. *Journal of Applied Meteorology and Climatology*, 50(1):185–202.

Ma, J., Liu, Q., et al. (2003). Flora of beijing: An overview and suggestions for future research. *Urban habitats*, 1(1):30–44.

Masson, V., Champeaux, J.-L., Chauvin, F., Meriguet, C., and Lacaze, R. (2003). A global database of land surface parameters at 1-km resolution in meteorological and climate models. *Journal of climate*, 16(9):1261–1282.

Minitab (2017). The minitab blog. regression analysis: How do i interpret r-squared and assess the goodness-of-fit? `http://blog.minitab.com/blog/adventures-in-statistics-2/`. [Online; data accessed 21-9-2017].

Mitchell, V., Cleugh, H., Grimmond, C., and Xu, J. (2008). Linking urban water balance and energy balance models to analyse urban design options. *Hydrological processes*, 22(16):2891–2900.

Nair, U. S., McNider, R., Patadia, F., Christopher, S. A., and Fuller, K. (2011). Sensitivity of nocturnal boundary layer temperature to tropospheric aerosol surface radiative forcing under clear-sky conditions. *Journal of Geophysical Research: Atmospheres*, 116(D2).

NASA (2010). Tiny particles - big impact. `https://earthobservatory.nasa.gov/Features/Aerosols`. [Online; data accessed 12-10-2017].

Offerle, B., Grimmond, C., and Fortuniak, K. (2005). Heat storage and anthropogenic heat flux in relation to the energy balance of a central european city centre. *International Journal of Climatology*, 25(10):1405–1419.

Oke, T. R. (1982). The energetic basis of the urban heat island. *Quarterly Journal of the Royal Meteorological Society*, 108(455):1–24.

Oke, T. R. (1987). *Boundary Layer Climates*. Routledge, Taylor and Francis Group, UK, London.

Petäjä, T., Järvi, L., Kerminen, V.-M., Ding, A., Sun, J., Nie, W., Kujansuu, J., Virkkula, A., Yang, X., Fu, C., et al. (2016). Enhanced air pollution via aerosol-boundary layer feedback in china. *Scientific reports*, 6.

Rodriguez, F., Andrieu, H., and Creutin, J.-D. (2003). Surface runoff in urban catchments: morphological identification of unit hydrographs from urban databanks. *Journal of Hydrology*, 283(1):146–168.

Rouse, W. R., Noad, D., and McCutcheon, J. (1973). Radiation, temperature and atmospheric emissivities in a polluted urban atmosphere at hamilton, ontario. *Journal of Applied Meteorology*, 12(5):798–807.

Running, S. W., Justice, C., Salomonson, V., Hall, D., Barker, J., Kaufmann, Y., Strahler, A. H., Huete, A., Muller, J.-P., Vanderbilt, V., et al. (1994). Terrestrial remote sensing science and algorithms planned for eos/modis. *International journal of remote sensing*, 15(17):3587–3620.

Sailor, D. J. (2011). A review of methods for estimating anthropogenic heat and moisture emissions in the urban environment. *International Journal of Climatology*, 31(2):189–199.

Schmid, H., Cleugh, H., Grimmond, C., and Oke, T. (1991). Spatial variability of energy fluxes in suburban terrain. *Boundary-Layer Meteorology*, 54(3):249–276.

Shao, M., Tang, X., Zhang, Y., and Li, W. (2006). City clusters in china: air and surface water pollution. *Frontiers in Ecology and the Environment*, 4(7):353–361.

Song, T., Sun, Y., and Wang, Y. (2013). Multilevel measurements of fluxes and turbulence over an urban landscape in beijing. *Tellus B: Chemical and Physical Meteorology*, 65(1):20421.

Spracklen, D. V., Carslaw, K. S., Merikanto, J., Mann, G. W., Reddington, C. L., Pickering, S., Ogren, J. A., Andrews, E., Baltensperger, U., Weingartner, E., et al. (2010). Explaining global surface aerosol number concentrations in terms of primary emissions and particle formation. *Atmospheric Chemistry and Physics*, 10(10):4775–4793.

Streets, D. G., Fu, J. S., Jang, C. J., Hao, J., He, K., Tang, X., Zhang, Y., Wang, Z., Li, Z., Zhang, Q., et al. (2007). Air quality during the 2008 beijing olympic games. *Atmospheric environment*, 41(3):480–492.

Sundström, A.-M. et al. (2014). Remote sensing of aerosols: Applications for air quality and climate studies. *Report series in aerosol science*, 158.

Sundström, A.-M., Kolmonen, P., Sogacheva, L., and de Leeuw, G. (2012). Aerosol retrievals over china with the aatsr dual view algorithm. *Remote sensing of environment*, 116:189–198.

Taylor, K. E. (2001). Summarizing multiple aspects of model performance in a single diagram. *Journal of Geophysical Research: Atmospheres*, 106(D7):7183–7192.

United Nations (2014). World urbanization prospects, the 2014 revision. [Pp.].

Van Donkelaar, A., Martin, R. V., Brauer, M., Kahn, R., Levy, R., Verduzco, C., and Villeneuve, P. J. (2010). Global estimates of ambient fine particulate matter concentrations from satellite-based aerosol optical depth: development and application. *Environmental health perspectives*, 118(6):847.

Vargo, J., Habeeb, D., and Stone, B. (2013). The importance of land cover change across urban–rural typologies for climate modeling. *Journal of environmental management*, 114:243–252.

Wallace, J. M. and Hobbs, P. V. (2006). *Atmospheric science: an introductory survey*. Elsevier, Amsterdam, 2nd edition.

Ward, H., Järvi, L., Onomura, S., Lindberg, F., and CSB, G. (2015). Suews manual: Version 2015a.

Ward, H. C., Kotthaus, S., Järvi, L., and Grimmond, C. S. B. (2016). Surface urban energy and water balance scheme (suews): development and evaluation at two uk sites. *Urban Climate*, 18:1–32.

WHO (2017). Air quality guidelines - global update 2005. `https://www.dieselnet.com/tech/dpm_size.php`. [Online; data accessed 17-8-2017].

Wikivoyage (2010). Beijing. `https://en.wikivoyage.org/wiki/Beijing`. [Online; data accessed 29-9-2017].

Xiao, Q., McPherson, E., Simpson, J., and Ustin, S. (2007). Hydrologic processes at the urban residential scale. *Hydrological processes*, 21(16):2174–2188.

Zheng, G., Duan, F., Su, H., Ma, Y., Cheng, Y., Zheng, B., Zhang, Q., Huang, T., Kimoto, T., Chang, D., et al. (2015). Exploring the severe winter haze in beijing: the impact of synoptic weather, regional transport and heterogeneous reactions. *Atmospheric Chemistry and Physics*, 15(6):2969–2983.

Appendices

A Site-specific model parameters

This Section comprises the used model site-specific parameters of the simulated 1 km radius circle around the Beijing tower, as well as general model run parameter options. The source for the chosen model variables are mostly the same as in Järvi et al. (2011) if not otherwise mentioned below the table. See Appendix B for notation explanations.

Table 11. Site specific model parameters used for the different surface types separately.

Parameter	Units	Paved	Buildings	Evergreen	Deciduous	Grass	Water
α_i	–	0.12	0.15	0.1	0.16[a]	0.19[a]	0.1
ε_i	–	0.91	0.95	0.98	0.98	0.93	0.95
S_i	mm	0.48	0.25	1.3	0.8	1.9	0.5
$D_{O,i}$	mm	10	10	0.013	0.013	10	–
b	–	3	3	1.71	1.71	0.013	–
$S_{soil,i}$	mm	150	150	150	150	150	–
a_1	–	0.719[b]	0.238	0.336	0.336	0.336	0.5
a_2	h	0.194[b]	0.427	0.313	0.313	0.313	0.21
a_3	W m^{-2}	-36.6[b]	-16.7	-31.4	-31.4	-31.4	-39.1
$g_{i,max}$	mm s^{-1}	–	–	7.4	11.7	40	–

[a] Vargo et al. (2013). [b]Calculated as an impervious average suitable for Beijing.

Table 12. General model parameter options.

Parameter	Value	Parameter	Value	Parameter	Value	Parameter	Value
SDD	-450	StateLimit	30000	SoilDepth	349	b_{0a}	-19.1853
$LAI_{min,everg}$	4	$T_{BaseGDD}$	5	K_s	0.0005	b_{1a}	2.2195
$LAI_{min,dec}$	1	$T_{BaseSDD}$	11	SoilDensity	1.16	b_{2a}	0.7836
$LAI_{min,grass}$	1.6	GDD	300	$G1$	3.5[d]	b_{0m}	-5.7556
$LAI_{max,everg}$	5.1	res_{drain}	0.25	$G2$	200[d]	b_{1m}	0.6658
$LAI_{max,dec}$	5.5	R_C	1	$G3$	0.13[d]	b_{2m}	0.2351
$LAI_{max,grass}$	5.9	res_{cap}	10	$G4$	0.7[d]	S_{pipe}	100
$b_1 = b_2$	0.04[c]	NARPTrans	1	$G5$	30[d]	K_{max}	1200
$c_1 = c_2$	0.001[c]	T_{BaseQF}	18.2	$G6$	0.05[d]	I_w	0.0
b_3	-1.5[c]	$\alpha_{0,\{wd,we\}}$	0.3081	T_H	55[d]	S_1	5.56[d]
c_3	0.0015[c]	$\alpha_{1,\{wd,we\}}$	0.0099	T_L	-10[d]	S_2	0[d]
RunoffToWater	0.1	$\alpha_{2,\{wd,we\}}$	0.0102				

[c]Järvi et al. (2014), [d]Ward et al. (2016)

B Abbreviations and model parameter notations

Model parameter notation and abbreviations used in this study in alphabetic order. The units are provided when possible.

α_i	Effective surface albedo
$\alpha_{0,\{we,we\}}$	Parameter defining the base value for Q_F per capita on weekends (*we*) and weekdays (*wd*), in W m^{-2} (capita^{-1} ha^{-1})$^{-1}$
$\alpha_{1,\{we,we\}}$	Parameter related to cooling degree days (CDD) on weekends (*we*) and weekdays (*wd*) when calculating Q_F, in W m^{-2} K^{-1} (capita^{-1} ha^{-1})$^{-1}$
$\alpha_{2,\{we,we\}}$	Parameter related to heating degree days (HDD) on weekends (*we*) and weekdays (*wd*) when calculating Q_f, in W m^{-2} K^{-1} (capita^{-1} ha^{-1})$^{-1}$
ε_i	Effective surface emissivity
a_1	OHM-coefficient for Q^* term
a_2	OHM-coefficient for dQ^*/dt term
a_3	OHM-coefficient constant term, in W m^{-2}
b	Empirical coefficient for the drainage equation. In this model the drainage equation was chosen to be Nr. 3 for all surface types (Ward et al., 2015)
$b_1(b_3)$	Coefficient (power) for leaf growth (off)
$b_{0a}-b_{2a}$	Coefficients for automatic irrigation model, in mm d^{-1}, mm d^{-1} °C $^{-1}$ and mm d^{-2}
$b_{0m}-b_{0m}$	Coefficients for manual irrigation model, in mm d^{-1}, mm d^{-1} °C $^{-1}$ and mm d^{-2}
$c_1(c_3)$	Constant in the leaf growth (off) equation, in °C
$D_{0,i}$	Drainage rate coefficient for each surface, in mm
$G1-G6$	Surface conductance parameters: G1 is related to maximum surface conductance (in mm s^{-1}), G2 is related to $K\downarrow$ dependence (in W m^{-2}), G3 & G4 are related to VPD dependence (in kg g^{-1} and g kg^{-1}), G5 is related to temperature dependence (in °C) and G6 is related to soil moisture dependence (in mm^{-1})
$g_{i,max}$	Maximum conductance for each vegetated surface, in mm s^{-1}
GDD	Growing degree days needed for fully capacity of the leaf area index, in °C
I_w	Flow change, difference in the water input and output for the water surface type, indicates the river flow through the grid, in mm h^{-1}
K_s	Saturated hydraulic conductivity of soil, in mm s^{-1}
K_{max}	Maximum incoming shortwave radiation, in W m^{-2}
$LAI_{max,I}$	Maximum LAI for vegetated surface type i, in m^2 m^{-2}
$LAI_{min,I}$	Minimum LAI of the vegetated surface type i, in m^2 m^{-2}. These values were used as initial condition values for the LAI due to the start of the run was in winter

R_C	Limit when the surface is totally covered with water in LUMPS, in mm
S_i	Maximum water storage capacity of the surface type i, in mm
S_{1-2}	Parameters related to surface conductance for S_1 (in $[-]$) and for S_2 (in mm)
S_{pipe}	Storage capacity of pipes, in mm
$S_{soil,i}$	Maximum storage capacity of the sub-surface soil store of the surface type i, in mm
T_H	Upper air temperature limit in calculating the surface conductance, in °C
T_L	Lower air temperature limit in calculating the surface conductance, in °C
$T_{BaseGDD}$	Base temperature for initiating growing degree days for leaf/vegetation growth of a vegetated surface, in °C
T_{BaseQF}	Base temperature for heating degree days in calculating Q_F, in °C
$T_{BaseSDD}$	Base temperature for initiating senescence degree days for leaf off for a vegetated surface, in °C
AHmin	Minimum Q_F, in W m^{-2}
AOD	Aerosol optical depth, a measurement of how polluted the air is by the optical depth, the thicker the more polluted is the air
LUMPS	Local-scale Urban Meteorological Parameterization Scheme, used for determining the atmospheric stability, needed for simulating the turbulent latent and heat fluxes (Q_e and Q_h)
LW	Long-wave radiation
NARP	Net All-wave Radiation Parameterization Scheme, used for calculating the net all wave radiation Q^*
NARPTrans	Atmospheric transmissivity in NARP
OHM	Objective Hysteresis Model, used for calculating the storage heat flux ΔQ_s
res_{cap}	Maximum water bucket reservoir / maximum surface water capacity in LUMPS, in mm
res_{drain}	Drainage rate of water bucket in LUMPS, in mm h^{-1}
RunoffToWater	Fraction of above-ground runoff that is flowing to water surface during flooding
SDD	Senescence degree days needed to initiate leaf off, in °C
SEB	Surface Energy Balance
SoilDensity	The soil density for all surface types, in kg m^{-3}
SoilDepth	Depth of the sub-surface soil store, in mm
StateLimit	Upper limit to the surface state, set only for the water surface, in mm
SUEWS	Surface Urban Energy and Water Balance Scheme, simple model for determining the different components in urban energy and water balance equations
SW	Short-wave radiation

C Data coverage of observed turbulent fluxes and aerosol data

Table 13. Daily coverage of turbulent fluxes measured at the height of 47 m as well as for AOD-data measured at the Beijing station for the study period of 2007 − 2009. The coverage is given considering the amount of missing data. This table gives the number of daily and hourly data points in both absolute and percentage values calculated for the total amount and divided into the thermal seasons as defined in Section 3.5.

	AOD (440nm) daily	Q_H **daily**	Q_E **daily**	**AOD (440nm) hourly**	Q_H **hourly**	Q_E **hourly**
Total missing	505	143	143	21990	4225	4282
Missing (%)	46.1	13.0	13.0	83.6	16.0	16.3
Winter missing	63	23	23	2605	707	695
Missing (%)	49.6	18.1	18.1	85.5	23.2	22.8
Spring missing	73	15	15	3487	532	540
Missing (%)	41.5	8.5	8.5	81.6	12.5	12.6
Summer missing	296	85	85	13000	2410	2487
Missing (%)	45.4	13.0	13.0	83.1	15.4	15.9
Autumn missing	73	20	20	2898	576	560
Missing (%)	52.5	14.4	14.4	86.9	17.3	16.8

Table 14. Hourly available data shown per pollution category and thermal season. The total absolute values are shown as well as the relative share (in brackets) in percentage for data coverage in each thermal season, separately. The superscripts 1−3 at the thermal seasons refers to which variable is analyzed: 1 stands for both modelled Q_H and Q_E with respect to available AOD-data. 2 refers to observed Q_H data taking into consideration both available AOD-data as well as observed Q_H. The superscript 3 counts for available data for Q_E similarly as for the previous one.

Thermal season	**AOD = 1**	**AOD = 2**	**AOD = 3**	**AOD = 4**	**Total**
Winter^1	37	83	152	171	443 (14.5)
Spring^1	196	192	244	153	785 (18.4)
Summer^1	728	622	834	464	2648 (16.9)
Autumn^1	72	71	131	164	438 (13.1)
Total^1	1033	968	1361	952	**4314 (16.4)**
Winter^2	20	67	88	116	291 (9.5)
Spring^2	177	189	220	127	713 (16.7)
Summer^2	561	552	699	412	2224 (14.2)
Autumn^2	70	71	120	145	406 (12.2)
Total^2	828	879	1127	800	**3634 (13.8)**
Winter^3	20	67	88	127	302 (9.9)
Spring^3	179	189	222	131	721 (16.9)
Summer^3	564	553	705	424	2246 (14.4)
Autumn^3	70	70	122	159	421 (12.6)
Total^3	833	879	1137	841	**3690 (14.0)**